STScI | SPACE TELESCOPE SCIENCE INSTITUTE

WFC3/UVIS External CTE Monitor: 2016 Updates on Coefficients and Analysis Pipeline

C.M. Gosmeyer & S. Baggett

March 15, 2017

ABSTRACT

The evolution of the charge transfer efficiency (CTE) of Hubble's WFC3/UVIS detector has been monitored since 2009, using observations of star clusters NGC 104 and NGC 6791. We present here results from an updated analysis pipeline with an improved cross-identification of sources and a new capability to study CTE loss mitigation by use of flash levels 6 - 116 e-/pix. We measure flux loss due to CTE degradation as a function of source brightness, observation date, background level, and vertical distance from the readout amplifier with a 2nd degree polynomial, whose coefficients are provided to allow observers to estimate flux corrections for their point-source photometry. Current flux losses for images with the recommended minimum 12 e-/pix background are 5 - 15%, depending on source brightness. These losses are further reduced via use of the CTE-corrected images now available from the Mikulski Archive for Space Telescopes. Within its overall growth, there appears to be a flattening in the CTE degradation rate that may be correlated with the Solar cycle maximum. The data reported here span from October 2009 to August 2016 and were calibrated with `calwf3 v3.3`*.*

1

Introduction

Cosmic rays degrade the silicon lattice of space-based CCD detectors (Janesick, 2001). This bombardment results in a continuous loss of charge transfer efficiency (CTE), a loss that impacts precision in photometry and astrometry. During readout, charge travels to the corner amplifiers. If the lattice is damaged, charge will get trapped, and this is seen in images as a "trailing" behind sources in the anti-direction of readout. Figure 1 illustrates that sources' trails are more extended the farther they are from the amplifiers. Because the effect was known on previous Hubble Space Telescope (HST) CCDs (WFPC2, ACS/WFC, STIS), the Wide Field Camera 3 (WFC3)'s two-chip CCD detector, UVIS, has been monitored for CTE degradation since its installation on HST in 2009. The degradation of CTE on WFC3 has been summarized in numerous reports (Noeske et al. (2012), Baggett et al. (2015)). Observers can correct for CTE loss by running on their images the pixel-based software (Anderson, 2011). Since 2016, another option available to users is to directly retrieve the CTE-corrected products from the Mikulski Archive for Space Telescopes (MAST).

Strategies to minimize flux losses due to CTE degradation are discussed in greater depth in other reports (Anderson et al. (2012), Noeske et al. (2012), Baggett et al. (2015), and Chapter 6 of Deustua (2016)). In brief:

- Place the source close to a readout amplifier. The signal will be impeded by fewer charge traps during readout.

- Increase background level, either by using a wider filter or by post-flashing the image, to at least 12 electrons per pixel. If the background is too low (i.e., more traps are empty), faint sources are at risk of being trailed out entirely.

- Increase source signal with exposure time or observe a brighter source altogether.

- Observe a denser scene. A source will suffer less flux loss if other sources fill charge traps before it during readout.

- Use archival images if appropriate. CTE degradation increases with time as the detectors continue to accumulate radiation damage.

This report introduces a new analysis of all the WFC3/UVIS external CTE monitor's data. It is an improvement over past reports for three primary reasons: (1) the data are re-calibrated from the 2016-released version of the calibration pipeline, `calwf3 v3.3`; (2) the analysis pipeline was re-written from `IDL`/`IRAF`/`FORTRAN` to mostly `Python` (retaining the `IRAF`-based photometry for this report) and implements an improved source matching strategy,

enabling us to more robustly measure CTE trends; (3) the relevant header information and photometric results are stored in a `SQLite` database, allowing us to easily expand analysis to new subsets of monitor data (e.g., the same-chip dataset described in Gosmeyer and Baggett (2016) and datasets with flash levels other than 12 e-/pix, studied for the first time in this report) that were prohibitively clunky to process in the structure of the old analysis pipeline.

After describing the data, the observation strategy, and the motivation, master catalogs and steps of the new analysis pipeline (with an aside comparing `Python`- to `IRAF`-based photometry), we discuss updated coefficients for the point-source photometric correction formula; CTE trends with time, including a suspected Solar cycle effect; CTE trends with flash level to study to the efficiency of the pixel-based CTE correction software (Anderson, 2011); and the source recovery from the uses of post-flash and the correction software. Appendix A tabulates the observations from each cycle. Appendix B compares the new and old analysis pipelines. Appendixes C and D contain additional plots for the non-nominal flash levels (6, 18, 24, 33, 55, 91, and 116 e-/pix).
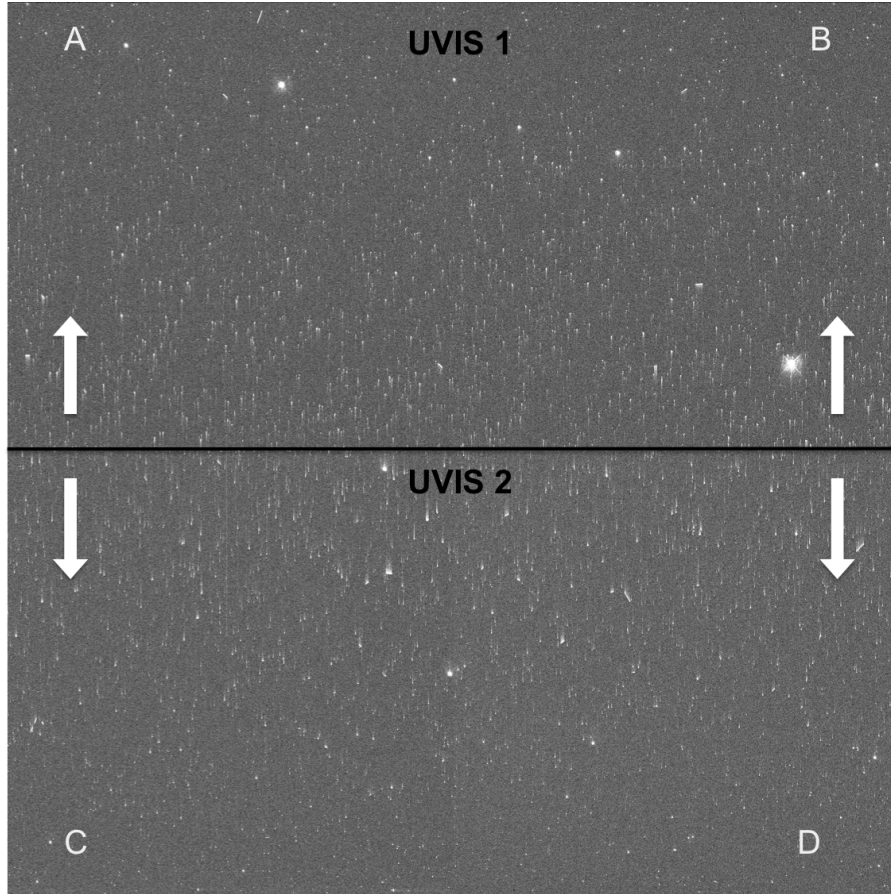

Figure 1 – Illustration of CTE loss on a WFC3/UVIS 60-second exposure, without post-flash or CTE correction, of NGC 6791 in 2015. The four amplifiers are labeled and arrows point in direction of readout.

Data

The WFC3/UVIS external CTE monitoring program is considered "external" because it observes astronomical targets instead of "internal" targets such as the EPER flats (Khandrika et al., 2016). HST time is precious and we justify applying each cycle for external observations because they more closely approximate science observations, and thus studies such as these can yield more immediate and practical results for observers. This program has many nuances that have evolved over the years and we describe only those that are relevant to this report's analysis. The targets are fields within two clusters of different relative densities: sparse NGC 6791 and dense NGC 104 (47 Tuc). The two densities allow us to study how CTE loss is affected by the pre-filling of traps during readout; that is, a crowded field should show less CTE loss, while a sparse field should give a more "pure" measure of CTE loss (Noeske et al., 2012). Until Cycle 20 (2012-2013) the clusters were observed with two filters, F502N and F606W, to provide low and high-background images, respectively. Following Cycle 20 and the new availability of the post-flash mode, all observations are taken only in F502N to free up time to take post-flashed images of each target. In addition, it was deemed unnecessary to continue F606W because post-flash could provide, as the use of two filters did, a variety of backgrounds against which to measure CTE loss. Filter F502N was chosen to remain because it has effectively no background. Both clusters sample two flash levels, 6 and 12 e-/pix, as well as no post-flash. Field NGC 104 samples additional levels of background, 33, 55, 91, and 116 e-/pix, by adjusting the flash exposure times. Starting in Cycle 23 (2015-2016), flash levels 18 and 24 e-/pix are also taken to provide a finer sampling of background levels. Flash level 12 e-/pix is most used in our analysis because it is the level recommended to observers for general use. Observations are taken with short ($\sim$30 s) and long ($\sim$350 s) exposure times.

The exposures are summarized in Tables 2 and 3 in Appendix A and drizzled images of the fields are shown in Figures 4 and 5, for NGC 104 and NGC 6791, resepectively.

Observation Strategy

In order to measure CTE loss as a function of y-distance from a readout amplifier, observations are taken in pairs dithered by a chip-height (2048 pixels). As illustrated in Figure 2, the field is first observed in UVIS2. The detector is then dithered in the y-direction in a 2048-pixel step, and an identical exposure of the same field is taken in UVIS1. A source that is near an amplifier in one chip will be further from an amplifier in the other chip. Since more flux is lost due to CTE degradation the further a source is from an amplifier,

we are provided with a measurement of CTE loss by ratioing the flux of the sources imaged on UVIS1 over the flux of the same sources imaged on UVIS2, and plotting the flux ratios against row number (y-position). See Figure 7 for examples of these plots. This method of observation is repeated for each combination of flash level, exposure time, and filter described in the Data Section. From 2010 to 2013, each field was observed three times a year. Starting in 2014 we decreased the cadence to twice each year for each field.

This method does have a bias, however. The CTE loss of the two chips is blended into a single measurement. In an ideal monitor, we would image the field in each chip, rotate the detector 180 degrees, and again image the same field in each chip. This would provide a measurement of CTE loss with y-distance from the amplifier for each chip individually. We have, in fact, recently analyzed a 2012 dataset (calibration proposal 12692) in which just such an observation strategy was implemented. The results are published in a companion instrument science report, Gosmeyer and Baggett (2016). We find that CTE degradation trends are similar between the two chips, but UVIS1's degradation is consistently higher than UVIS2's by, at maximum, ∼3% to ∼17% fractional flux loss/2048 pixels, for CTE-corrected, non-post-flashed, 348- and 60-second exposures, respectively. This per-chip measurement is more difficult to schedule, unfortunately, because image pairs must be taken following a 180-degree roll of the telescope within a space of a few days, and thus, is not expected to be performed often. Instead, we use the method described in this report, shifting the target scene from one chip to the other.
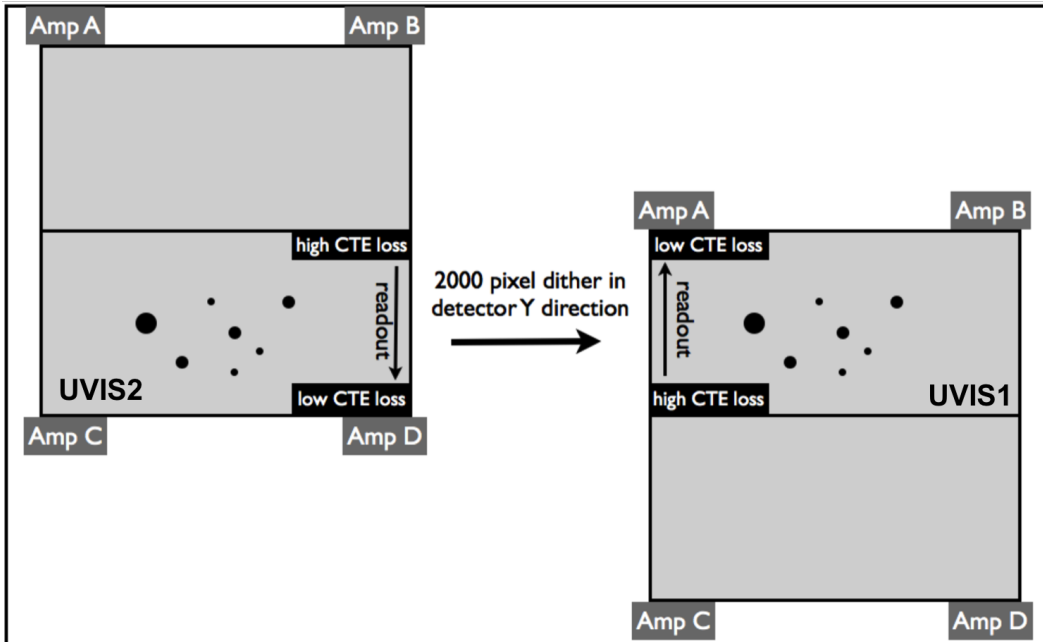

Figure 2 – Strategy of observations for measuring CTE loss. Reprinted from Noeske et al. (2012).

Motivation to Re-write the Analysis Pipeline in Python

We re-wrote the external CTE monitor's analysis pipeline from `IDL/IRAF/FORTRAN` to `Python`. We were motivated by several factors.

1. The algorithm for matching sources between a pair's images was no longer ideal for the data. To overlap the images, the algorithm rotated and shifted them in pixel space, and the number of pixels shifted was hard-coded, so it needed assume the dither between pairs was exactly the same each time. Sources, identified with `IRAF/DAOFIND`, were matched between chips based on how closely, within a set radius, the center of a source on one chip overlapped with the center of a source on the other chip. This algorithm worked well in early epochs before sources trailed considerably from CTE loss. As CTE degradation worsened, this method identified reliably fewer and fewer real sources, especially in the lowest flux bins, because their flux trails were too severe for the algorithm to recognize them as point sources. This method also had the downside that it often allowed cosmic rays and diffraction spikes to be identified as sources and bright stars as many sources. Further, it was not possible to track just a single source accurately in multiple image pairs because its only identifier was an x, y coordinate in pixel space unique only to each image. Our new matching method is an improvement over the old because it matches sources to master catalogs using RAs and Decs. A single source can then be confidently tracked through time and mis-identified sources can be minimized. The next section describes the creation of the master catalogs. Close inspection between old and new plots in Figure 3 reveals many of the NGC 104 "sources" marked with the old pipeline's matching algorithm are cosmic rays or diffraction spikes, and even true sources marked on one image are not marked on the other. All the marked sources with the new pipeline are exactly the same between images in the pair. About five of the brightest stars are left out of the NGC 104 catalog since they tend to saturate in the long exposures.
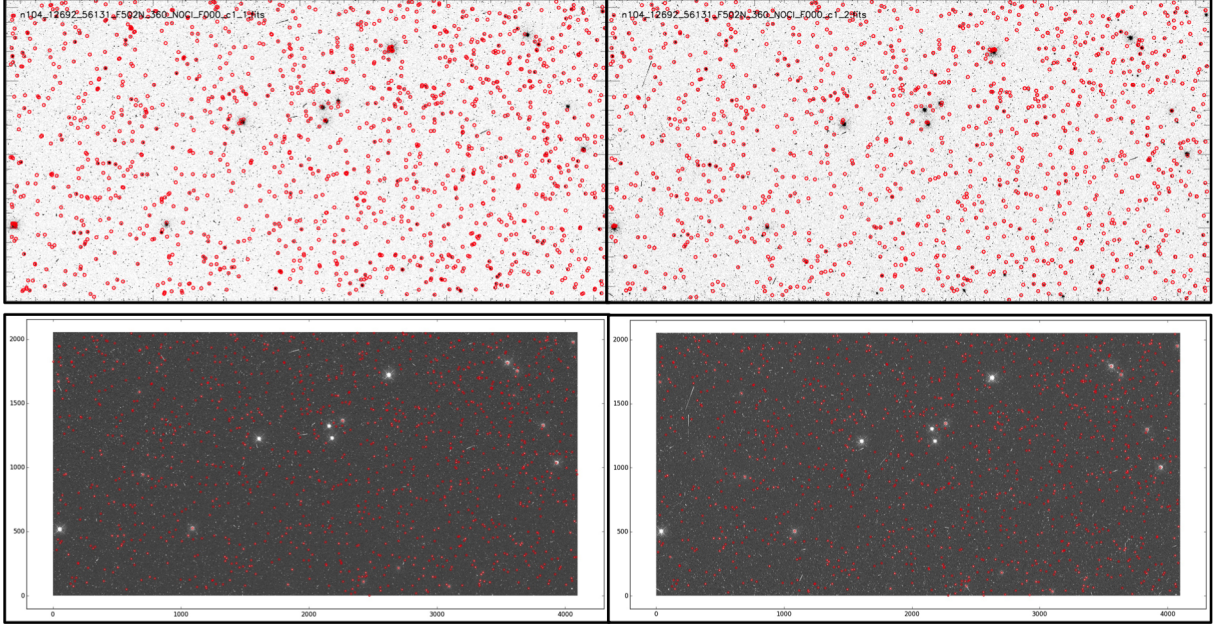
Figure 3 – Example diagnostic images with matched sources overplotted from the old pipeline (top) and the new pipeline (bottom). They are from one pair, `ibwb08a2q` and `ibwb08aeq`, proposal 12692, target NGC 104, filter F502N, exposure time 360 seconds.

2. The types of studies we wished to perform were outgrowing the structure of the pipeline, making our analysis time-consuming as we re-fit the code for each case. For example, we wished to run the pipeline over the non-nominal flash level images, but much of the pipeline was hard-coded for just 12 e-/pix or no post-flash. Some datasets were impossible to analyze without overhauling the structure entirely; see, for instance, our study of the same-chip dataset in Gosmeyer and Baggett (2016). And because the pipeline was a combination of various languages, such as `IDL`, `Fortran`, and `IRAF`, written by various authors, maintenance was difficult. The new pipeline is written purely in `Python` (with the exception of the photometry, which is called from within `Python` using the `IRAF` wrapper, `PyRAF`), is documented according the PEP 257 docstring standards, was kept general so that non-nominal datasets can be processed easily by setting a few parameters, and the number of documentation, code-containing, and parameter-setting files was cut from about 90 to 35. We hope this will make the pipeline more accessible for our team-members, as well as easier to maintain for anyone who may inherit it from us. We had additional motivation to step away from `IDL` because of the cost of licenses and from `IRAF` because it will eventually be unsupported.

3. In the old pipeline, CTE measurements were stored in an `IDL` structure. Filtering out a specific set of entries over this monitor's wide parameter space was non-trivial. In the new pipeline we store relevant image header information, photometry results, and CTE

measurements in a `SQLite` database. It has the benefit that it is a universal format that can be accessed not only from within `Python` but also from other languages and directly from the terminal. To query it a user does not need to know `Python`. Knowledge of only a few `sql` commands is necessary. Querying the database for a specific entry is fast, and at least for us, more intuitive than filtering out results from the `IDL` structure.

We compare the CTE measurements of the two pipelines in Appendix B.

Creating the Master Catalogs

Our UVIS1-to-UVIS2 source-matching algorithm depends on a master catalog of RAs and Decs. We create a master catalog for each field, one in NGC 104 and the other in NGC 6791, by drizzling six early-epoch (i.e., with little CTE loss), long-exposure, F502N FLC images for each field and running the `PyRAF` call of `IRAF/DAOFIND` over them. The drizzled images are shown in Figures 4 and 5. The NGC 104 images are from 2012 and the NGC 6791 images are from 2010. We overplotted the identified sources onto the drizzled images and rejected all false identifications from the chip gap, edges, and so on. The final catalog for the NGC 104 field contains ∼3000 sources and for the NGC 6791 field, ∼1000 sources. Any given exposure contains about 1/3 of the catalog's total sources. A similar method using a master drizzled image is employed by the HST/ACS team for their external CTE monitor (Chiaberge, 2012). We chose F502N to create the master catalogs because F606W was discontinued in Cycle 20. For the reasons described in Appendix B, we may eventually create additional catalogs from F606W.

We do not take proper motion into account at this time. Re-centroiding the sources during the photometry step seems to identify the peak center pixel fairly well in the `IRAF/DAOPHOT` photometry. The `Python/Photutils` photometry package lacks an easily implemented centroiding function, and we find that when we compare the results of the `Photutils` photometry to the those of `DAOPHOT`, with the settings as identical as we can make them, the centers are not being captured as well in the aperture radii of the `Photutils` photometry. Future work will both look into implementing centroiding into the `Python`-based photometry and incorporating proper motions into the RAs and Decs. Proper motion will become a bigger concern as the monitor continues. The original `IDL` pipeline was robust against proper motion because it did not use a master catalog. The fact that our results come close to the `IDL` pipeline's (see Appendix B) gives us confidence that, for now, re-centroiding in `IRAF/DAOPHOT` is overpowering the effects of proper motion.
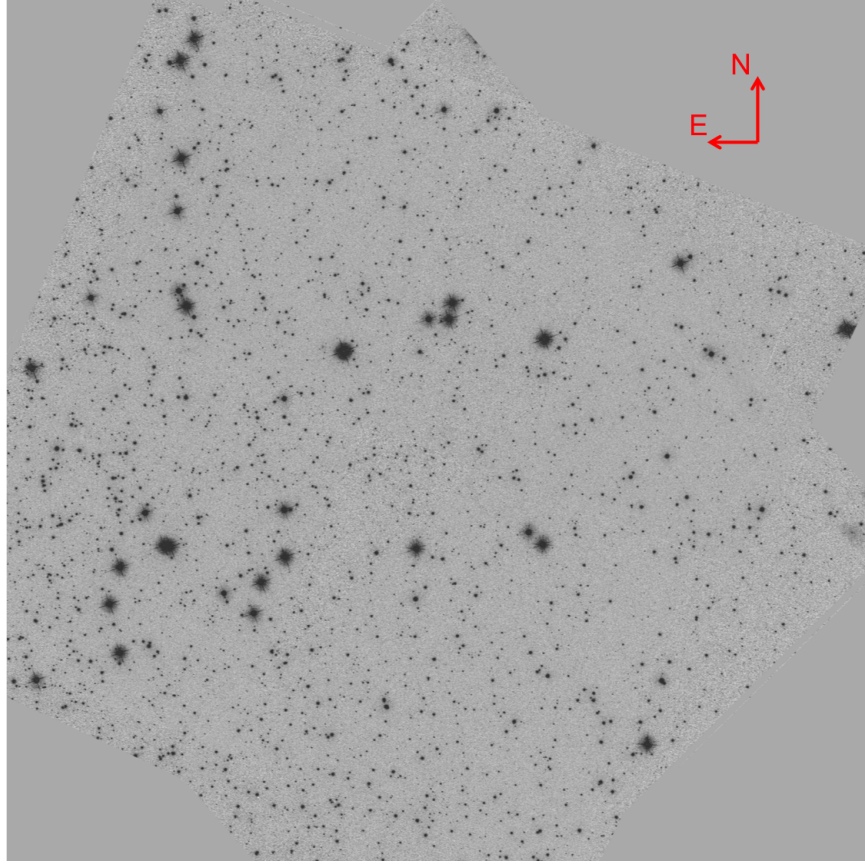
Figure 4 – The NGC 104 master drizzled image, from which we derived the master catalog of the field. The image is composed of six F502N, 360-second, CTE-corrected images: `ibwb02eiq_flc.fits`, `ibwb02eoq_flc.fits`, `ibwb05dlq_flc.fits`, `ibwb05drq_flc.fits`, `ibwb08a2q_flc.fits`, *and* `ibwb08aeq_flc.fits`.
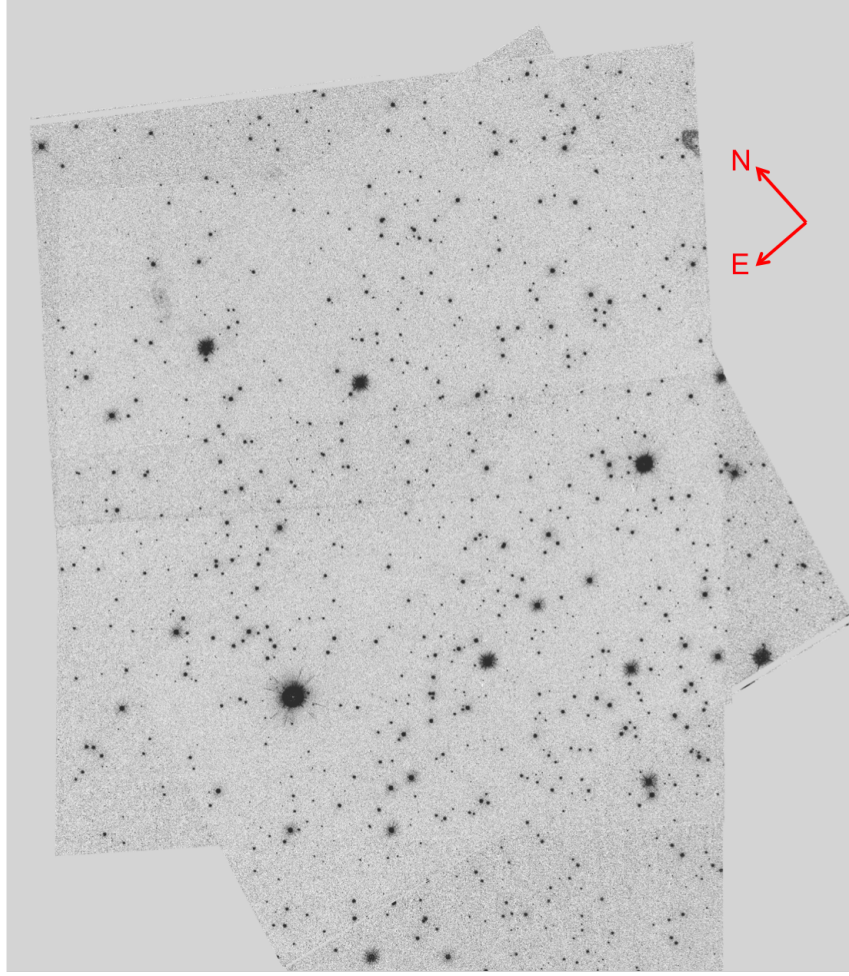
Figure 5 – The NGC 6791 master drizzled image. It is composed of six F502N, 420-second, CTE-corrected images: `ibc602uvq_flc.fits`, `ibc602uxq_flc.fits`, `ibc603zgq_flc.fits`, `ibc603ziq_flc.fits`, `ibc601grq_flc.fits`, *and* `ibc601gtq_flc.fits`.

Steps of the Analysis Pipeline

Before we run the `Python` pipeline on a new epoch of exposures, we must complete some preliminary tasks.

We retrieve a new dataset of calibrated images (FLTs) and CTE-corrected calibrated images (FLCs) from The Mikulski Archive for Space Telescopes (MAST). We place the images in a staging directory and visually inspect them for anomalies. Next we shift the WCS of the new images to match that of the field's master drizzled image using the `drizzlepac.tweakreg` function `TweakReg`. We then inspect the `TweakReg` diagnostic plots.

For the analysis in this report, we re-retrieved from MAST the images from all of the monitoring proposals going back to 2009 so that they all would be calibrated with the latest

version of the WFC3 calibration pipeline, `calwf3 v3.3` (Ryan, Jr. et al., 2016).

Note that we do not reject cosmic rays. Cosmic-ray cleaning software such as `L.A.Cosmic` (van Dokkum, 2001), which replaces pixels flagged as cosmic rays with a median of the neighboring good pixels, might contaminate our measure of CTE loss. We performed a short exercise where we compared photometry between an original and a cosmic-ray-cleaned image. Results suggest that the cleaning removes too much flux, and the ensuing CTE loss slopes do not show the gradual flattening with increasing source flux that we would expect. The unpromising results may be alleviated by a finer tuning of the software's parameters or by employing other means for cosmic-ray cleaning (e.g., `AstroDrizzle`). We would expect the scatter to decrease in a well-cleaned image and we may, with that expectation, look further into it this year.

With the preliminary steps complete, we are ready to run the pipeline on the FLTs and FLCs, both using the same master catalogs. The exact same steps are applied to an FLT as they are to an FLC; at the end we want the two to be directly comparable, so to evaluate the efficiency of the CTE correction software. A general run of the pipeline is to accomplish four primary tasks: (1) match RAs and Decs of known sources in the master catalogs to each image and return a coordinate file of sources, (2) run photometry on the sources, (3) match image pairs and from their sources' flux differences measure CTE loss, and (4) output publishable plots. We break down the pipeline's steps below.

1. Read each image's header and store information on its target star cluster, flash level, exposure time, observation date, filter, whether FLT or FLC, and target chip number, identified using the POSTARG1 header keyword.

2. Place the known sources, using RAs and Decs, from the target field's master catalog onto the image. We are able to reliably overlay the master catalog because we tweaked the WCS of the image to the master catalog's (which also corrected geometric distortion). The function `drizzlepac.skytopix.rd2xy` is then run to transform the RAs and Decs of sources to the image's pixel coordinates, which are needed for the measurement of CTE loss. A diagnostic figure in `PNG` format is created in this step as well, overlaying circles on the image where the catalog believes sources to be. Examples are shown in Figure 3. We inspect these for offsets.

3. Perform photometry on the sources by invoking the `IRAF`/`DAOPHOT` task `PHOT`. We do many aperture radii (14 radii between 2 and 40) and danulii of 10 pixels to find local background. An aperture of 3 pixels is used primarily in this report's analysis because the fields are crowded - larger apertures allow in too many contaminating sources. We expect some of the apertures will contain cosmic rays because we do not perform any cosmic-ray rejection. Before running the photometry function on an FLT or FLC, the pipeline applies

the chip-specific pixel area maps to correct for the detector's unequal pixel areas (WFC3 Team, 2009).

We found during the writing of this report that the `IRAF/DAOPHOT` task `PHOT` (whether called from `PyRAF` or not) and the `Python/Photutils` function `aperture_photometry` yield different flux counts at very small aperture radii. Figure 6 illustrates the discrepancy which, by 3 pixels, falls below 1% and, by $\sim$7 pixels, becomes negligible. The `PHOT` task is, in fact, approximating the area (Davis, 1987), while the `aperture_photometry` function, with the *method* parameter set to "exact," counts flux from the exact πR^2 area. At a 3-pixel radius in our data, we have seen the area varying by under 1% from the mean area to (more rarely) up to 20%, which leads to areas between 28.278 pix^2 at minimum to 28.842 pix^2 at maximum. The actual area should be 28.274 pix^2 – which is lower than even the minimum calculated by `PHOT`. Note that `PHOT` does, in fact, report the correct area of its approximated apertures in the output files, but one cannot just assume that the area is exactly πR^2. Results from our photometry tests on a simulated 2-D gaussian star are shown in Figure 6. The ratios of `IRAF`- to `Python`-calculated area and flux show that the `PHOT` task is, in most cases, over-approximating the aperture area, and hence counting additional flux, over 4% until about a 2-pixel radius. Afterward the ratio bounces around <1% until $\sim$7-pixel radius. Note that the area approximation also depends on the centering of the source in a pixel and the area can (though rarely) vary more than the <1%. Based on this analysis, it is not recommended that users of `IRAF` photometry use aperture radii less than 3 pixels. The `Python/Photutils` to `IRAF/DAOPHOT` discrepancy is reported in more detail in Bajaj and Khandrika (2017).

We are able to switch between `Python/Photutils` and `IRAF/DAOPHOT` photometry in our analysis pipeline. But we decided for the time being to report only the `PHOT` results for consistency with the `IDL` pipeline's photometry, which also used the `IRAF/DAOPHOT` task `PHOT`. In addition, the `Python/Photutils` functions are somewhat underdeveloped for our needs. We needed to write wrappers around them to bring their functionality up to that of `IRAF/DAOPHOT` and we are not yet satisfied with some aspects, such as centroiding (discussed in the section Creating the Master Catalogs). We will continue to improve our wrappers, as it is our goal to move the pipeline entirely to `Python`.
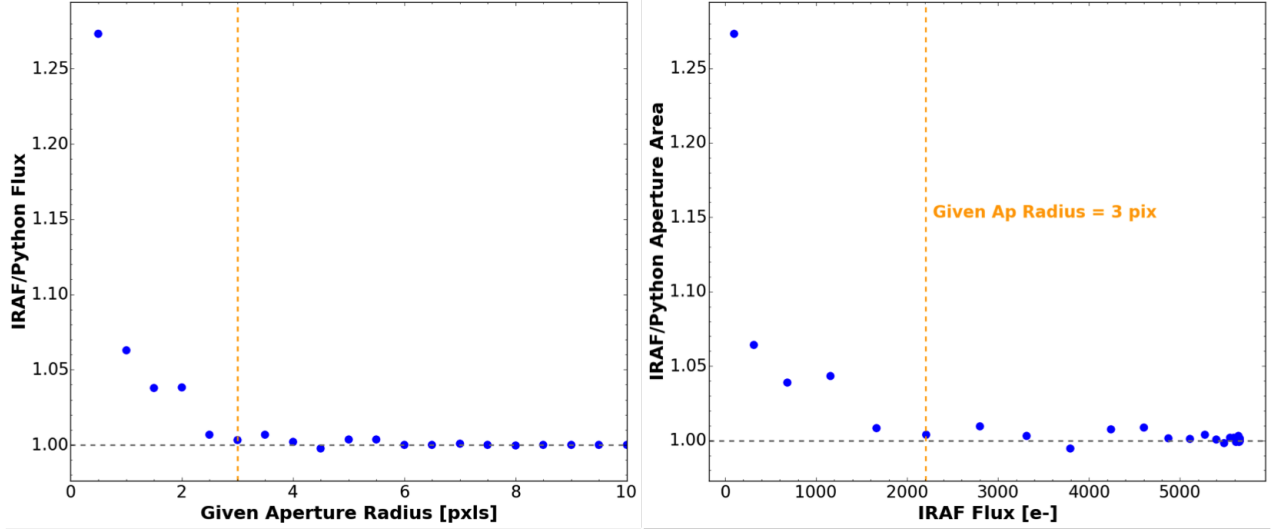
Figure 6 – Comparing `IRAF/DAOPHOT` *with* `Python/Photutils` *photometry on a simulated 2-D gaussian star, without background. In this report we use aperture 3 pixels, denoted here by the dashed horizontal orange lines.*

4. Insert the header information and the photometry results into the database. The database consists of a separate table for each target. The rows of the header information tables are sorted by image name. The rows of the photometry tables are sorted by image name, the master catalog's ID of the source, and aperture radius.

5. Pair the images after all the photometry on the new images is completed. The file information table of the database is queried for two images whose parameters listed in Step 1 match, differing only in the chip number.

6. Measure the CTE loss from each image pair. This is accomplished by taking the ratio of the background-subtracted flux of each source on UVIS1 over the flux on UVIS2, and plotting the flux ratios against the source's UVIS2 y-distance, in pixels, from the readout amplifier. In order to see how CTE changes with source brightness, the flux ratios are separated into eight flux bins ranging from 250-500 to 8000-32000 e-. Each bin is three-sigma clipped to remove outliers. A linear fit is then applied to the scatter plot resulting from each flux bin (see Figure 7 for examples) and the slope of the fit is stored in the database for further analysis. To obtain a CTE measurement in flux / 2048 pix, we divide this slope by 2 and multiply by 2048. We then have a measure of CTE degradation in units of flux over pixel y-distance from the readout.

In addition to illustrating our method of measuring CTE loss, Figure 7 depicts how CTE has degraded with time. The plot on the left is from 2010 and on the right from 2015, identical in all parameters except for observation epoch. All the slopes from the earlier epoch are fairly flat, indicating little CTE loss at even the lowest flux bin. In contrast, the

later epoch on the right shows large flux loss in the low flux bins (grey, green, blue), and little flux loss in the highest flux bins (orange, red, pink).

If one assumes that CTE losses at the centers of both chips are roughly the same and that the alignment of the scene on both chips in a pair are perfect, a source that falls in the center of the pair should experience the same CTE losses on both chips, and therefore, have a flux-ratio of 1.0. However, as one can see in Figure 7, the flux-ratio is not always 1.0 at the center (y-position of 1024 pixels). This is due to flaws in our simple assumption. First, even with perfect alignment and exactly the same central CTE losses, the flux-ratio could deviate from 1.0 because of flat-field variations, cosmic rays in the photometric aperture, and so on. Second, just from blinking the image pairs, we know that the alignment is not perfect, so a source in the center of one chip is often offset by a few pixels in the other chip. Finally, and perhaps the most overwhelming reason for the mismatch, is that the two UVIS chips were cut from different wafers, and thus some of their properties, such as their initial distribution of charge traps, are different (WFC3 CCD Milestone Review, 2001). The ACS/WFC external CTE monitor fixes the fit so that it always crosses at 1.0 and ACS team is able to justify that because the two ACS/WFC chips, unlike WFC3/UVIS, were cut from the same wafer (Chiaberge, 2012). Since we cannot provide such a justification, we leave the fit untouched. We will in the future investigate fixing the fit for the same-chip dataset described in Gosmeyer and Baggett (2016) and perhaps cut down the uncertainties of those measurements.

Further, we do not expect that all sources will show a clean CTE-induced decrease in flux with distance from the amplifier. Flux variations can also be caused by astronomical and unrelated instrumental effects. The impact of these fluctuations is limited by that image pairs are observed within 24 hours of each other and the number of sources is large. Sources will be rejected from the final output if their flux in one of the pairs should fall out of the bin, such as from a cosmic ray hit. This method does lead to more scatter in the wider bins, such as 500-8000 e-, than in the narrower bins, such as 500-1000 e-.

7. Finally, plot the CTE measurements against other parameters, such as time and background. These plots are discussed in the next section.
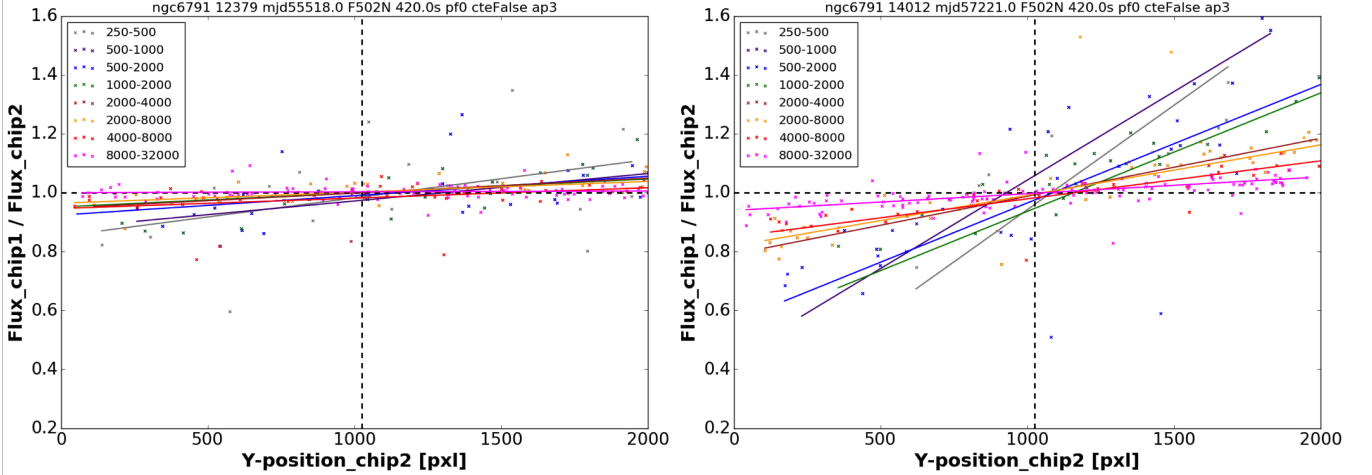
Figure 7 – Example plots of UVIS1 to UVIS2 flux-ratio vs y-position. The dashed vertical line indicates the center of UVIS2, y = 1024 pixels. The slope colors indicate bins of flux, ranging from 200-500 e- to 8000-32000 e-. In both plots, the target is NGC 6791, the aperture radius for photometry is 3 pixels, the exposure time is 420 s, the filter is F502N, and no pixel-based CTE correction has been applied. The only difference is the observation epoch of the image pairs. The plot on the left shows a pair (`ibnh01zhq_flt.fits` and `ibnh01zfq_flt.fits`) from Proposal 12379, November 2010. The plot on the right shows a pair (`icqu03y4q_flt.fits` and `icqu03xbq_flt.fits`) from Proposal 14012, July 2015.

Results and Discussion

We plot CTE loss as functions of source flux, time, and flash level, and derive new coefficients for the photometric correction formula. Each is discussed in a subsection below.

Photometric Correction Formula

In certain cases, photometry may be better corrected by the photometric correction formula rather than by the pixel-based software in order to retain a lower noise level or to obtain a more reliable (and not over-corrected) value; see, for example, Figure 18 in Appendix C. We derive coefficients for the photometric correction formula by plotting CTE loss against log10 flux (where $flux$ is actually the average of each flux bin depicted in Figure 7). To obtain a good fit to the majority of the points, we discarded the first flux bin before applying the fitting function. The CTE loss vs log10 flux plots are grouped by target and exposure length. NGC 104 long exposure plots are in Figure 8 and short exposure plots are in Figure 9, while the NGC 6791 long exposure plots are in Figure 10 and short exposure plots in Figure 11 . They are further divided by whether the observations were post-flashed with 12 e-/pix and whether they were corrected with the CTE correction software (Anderson,

2011). Additional flash levels (6, 18, 24, 33, 55, 91, and 116 e-/pix) for NGC 104 are plotted in Figures 20 - 26 in Appendix C. Observers can use these plots to estimate the flux loss due to CTE degradation in their aperture photometry.

Observers can also estimate the CTE-induced flux loss S, in units of e-/2048 pixels, with the equation

$$S = \sum c_{ij} d^i f^j \tag{1}$$

which expands to

$$S = c_{00} + c_{01}f + c_{02}f^2 + d \cdot (c_{10} + c_{11}f + c_{12}f^2) + d^2 \cdot (c_{20} + c_{21}f + c_{22}f^2) \tag{2}$$

where the source flux is $f = log_{10}(flux[e^-])$, observation date is $d = MJD - 55400$, and the fit's polynomial coefficients are c_{ij}.

Observers can then use the CTE loss estimate from Equation 2 to approximate the CTE-corrected flux of their aperture photometry using the following equation.

$$f_{corr}[e^-] = f_{uncorr}[e^-] + \frac{S}{2.5} \cdot \frac{Y}{2048} \tag{3}$$

where f_{uncorr} is the uncorrected source flux in e-, S is the CTE loss from Equation 2, and Y is the source distance from the readout amplifier in pixel rows. The latest F502N coefficients are in Table 1. Observers should use coefficients derived from conditions that most closely match their data, with matching the background levels being the first and foremost consideration. The top half of the table lists coefficients derived from non-CTE-corrected data and the bottom half from CTE-corrected data. Refer to http://www.stsci.edu/hst/wfc3/ins_performance/CTE/ for the latest F606W coefficients. Since observations for this filter were discontinued in 2012, we are not including them in new reports.

For further discussion of the photometric correction formula see Noeske et al. (2012), where it should be noted that Equation 4 is given with flux in magnitudes while here it is in electrons. There is a typo in Equation 2 of Noeske et al. (2012) and Baggett et al. (2015). The correct form, used in both the IDL and Python pipelines, is shown here in Equation 2.

We verify the modeled CTE loss by calculating from Equation 1 a value at each epoch for which we have observational values and plotting the model slopes against epoch over the observationally-derived measurements. We do this for three flux bins, using the average of the bin as the input flux for the formula. Results using the latest Python and IDL coefficients are shown in Figures 18 and 19, respectively. For both formulations, the model reproduces the higher flux bins well, but underestimates CTE loss for the lowest flux bin. The model, whether from the Python or IDL pipeline, fits observations best when the background is

12 e-/pix. Observers should be cautious when applying it to low-flux sources. It is likely the fit on the low-flux bins will continue to worsen as fewer sources fall into them due to CTE degradation. If the observation is from an earlier epoch and the source's flux and background are low, users may consider using earlier coefficients available online at http://www.stsci.edu/hst/wfc3/ins_performance/CTE/.
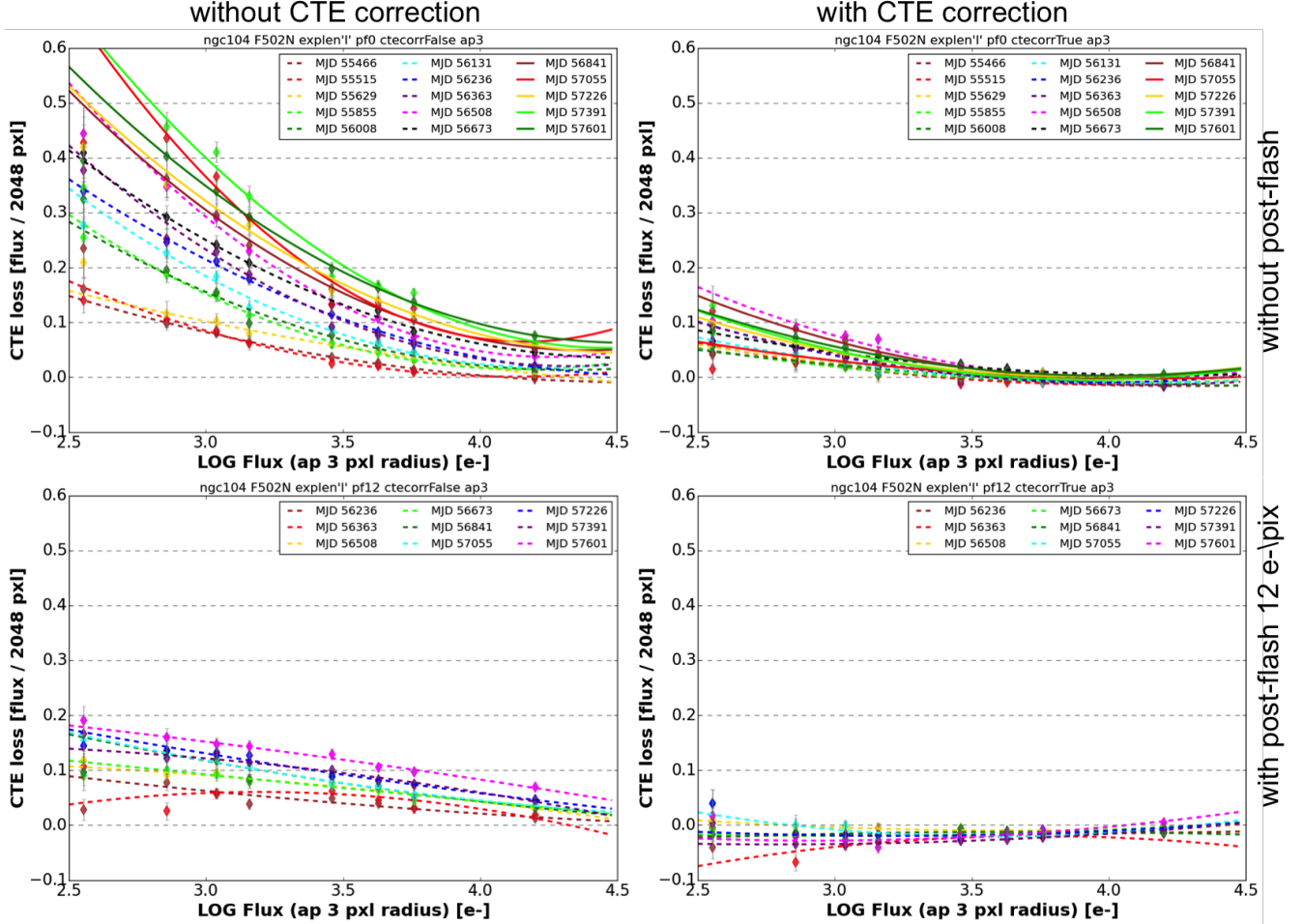

Figure 8 – Long-exposure plots for NGC 104 of CTE loss (in flux counts per 2048 pixels) vs log10 of the average of each of the eight flux bins. The points are fitted with 2nd degree polynomials. The left panels show values without CTE correction. The top panels show values without post-flash and the bottom panels show values with post-flash, where backgrounds are roughly 12 e-/pix.
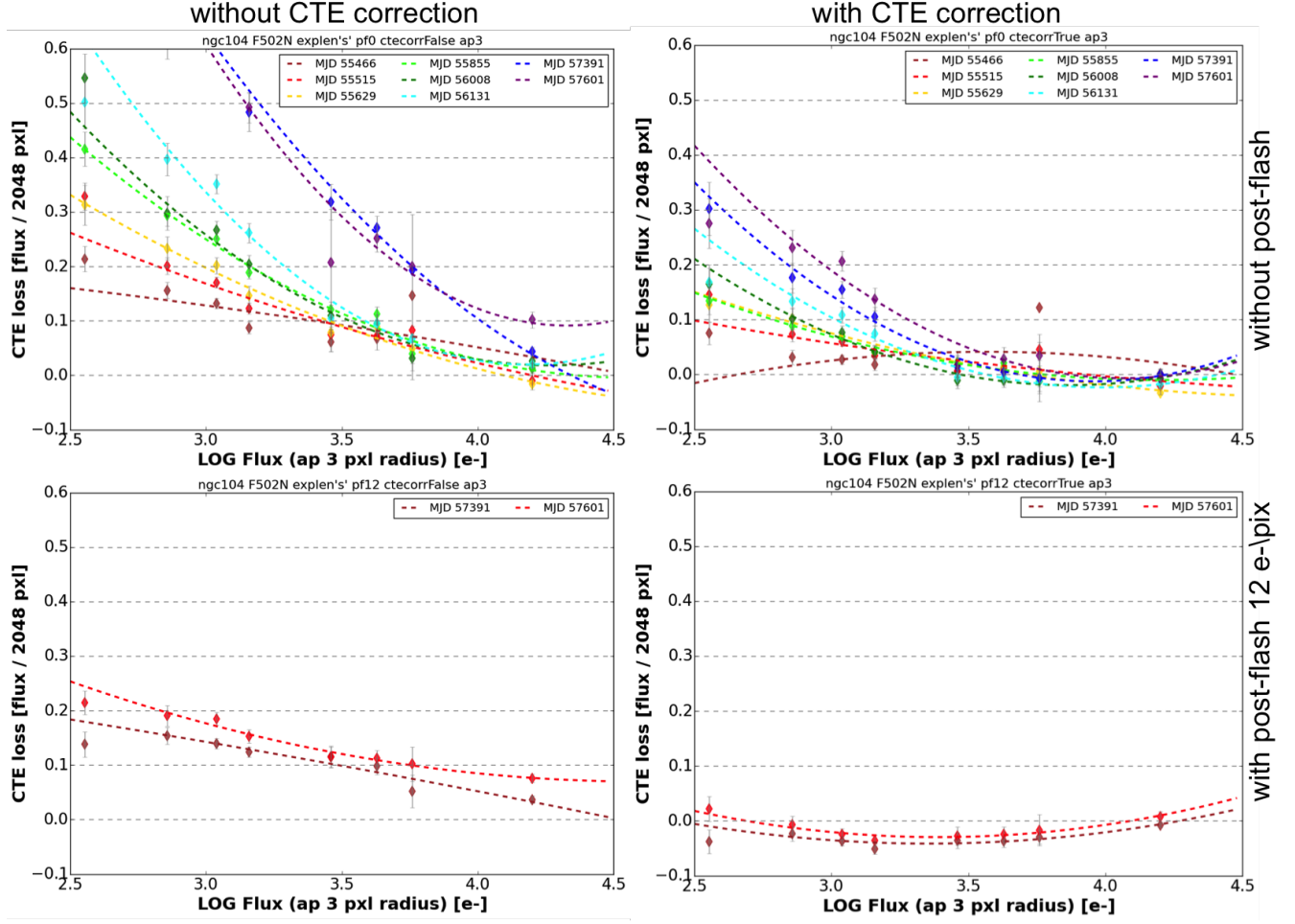
Figure 9 – Short-exposure plots for NGC 104. See the description of Figure 8. The plots of post-flash results show fewer epochs because we only started including short-exposure post-flash observations for the monitor in this past cycle.
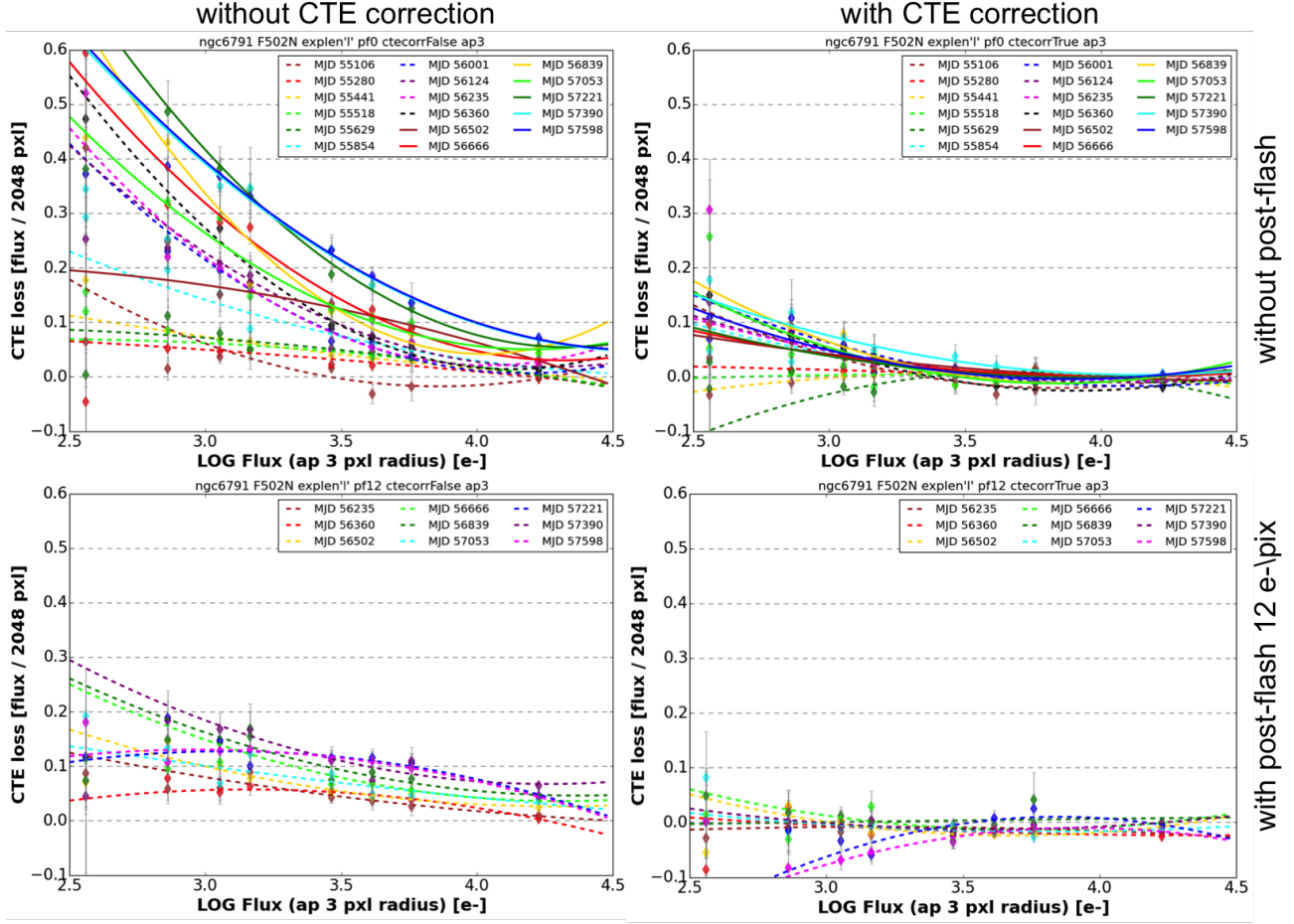
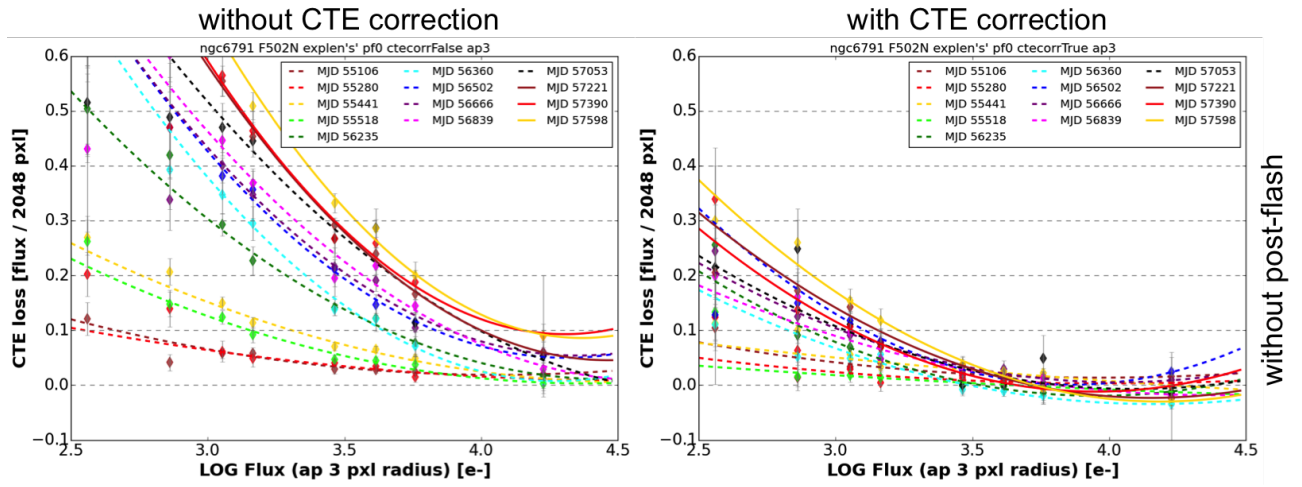*Figure 10 – NGC 6791, long exposure. See the description of Figure 8.*

Figure 11 – NGC 6791, short exposure. See the description of Figure 8. Note that no post-flashed short-exposure observations of NGC 6791 have been taken in this monitor.

19

	NGC 104					NGC 6791		
Flashlvl [e-/pix]	0	0	6	12	12	0	0	12
Exptime [s]	30	348	348	30	348	60	420	420
Bkgrd [e-/pix]	~0	~1-2	~5-11	~6-12	~6-12	~0	~1-2	~6-12
C00	2.37e-13	1.09e-13	4.91e-14	4.05e-14	1.20e-14	2.60e-13	1.23e-13	-1.51e-14
C01	-1.08e-13	-4.71e-14	-1.96e-14	-1.63e-14	-1.04e-15	-1.17e-13	-5.22e-14	1.39e-14
C02	1.24e-14	5.20e-15	2.03e-15	1.77e-15	-2.71e-16	1.34e-14	5.65e-15	-2.34e-15
C10	5.22e-10	2.41e-10	1.08e-10	8.91e-11	2.65e-11	5.70e-10	2.70e-10	-3.31e-11
C11	-2.37e-10	-1.04e-10	-4.31e-11	-3.59e-11	-2.29e-12	-2.57e-10	-1.15e-10	3.06e-11
C12	2.74e-11	1.15e-11	4.46e-12	3.90e-12	-5.96e-13	2.95e-11	1.24e-11	-5.15e-12
C20	1.15e-06	5.30e-07	2.38e-07	1.96e-07	5.83e-08	1.25e-06	5.93e-07	-7.28e-08
C21	-5.22e-07	-2.28e-07	-9.48e-08	-7.90e-08	-5.04e-09	-5.66e-07	-2.52e-07	6.72e-08
C22	6.03e-08	2.52e-08	9.82e-09	8.58e-09	-1.31e-09	6.48e-08	2.73e-08	-1.13e-08
C00	1.21e-13	3.68e-14	2.64e-14	2.81e-14	6.73e-15	1.05e-13	4.34e-14	-5.15e-14
C01	-5.98e-14	-1.84e-14	-1.43e-14	-1.73e-14	-5.42e-15	-5.09e-14	-2.24e-14	2.60e-14
C02	7.35e-15	2.31e-15	1.91e-15	2.56e-15	9.27e-16	6.08e-15	2.89e-15	-3.30e-15
C10	2.67e-10	8.11e-11	5.81e-11	6.19e-11	1.48e-11	2.31e-10	9.54e-11	-1.13e-10
C11	-1.32e-10	-4.05e-11	-3.15e-11	-3.82e-11	-1.19e-11	-1.12e-10	-4.93e-11	5.71e-11
C12	1.62e-11	5.08e-12	4.21e-12	5.63e-12	2.04e-12	1.34e-11	6.34e-12	-7.25e-12
C20	5.88e-07	1.78e-07	1.28e-07	1.36e-07	3.26e-08	5.09e-07	2.10e-07	-2.49e-07
C21	-2.90e-07	-8.91e-08	-6.92e-08	-8.40e-08	-2.63e-08	-2.46e-07	-1.08e-07	1.25e-07
C22	3.56e-08	1.12e-08	9.27e-09	1.24e-08	4.49e-09	2.94e-08	1.39e-08	-1.59e-08

Table 1 – Coefficients for F502N, NGC 104 (crowded field) on the left and for F502N, NGC 6791 (sparse field) on the right. The CTE-corrected values are in the bottom half. The coefficients are also available as text files from http://www.stsci.edu/hst/wfc3/ins_performance/CTE/.

CTE Evolution with Time

We plot the flux loss due to CTE degradation in e- per 2048 pixel rows against time in Modified Julian Date (MJD) for three flux bins. Figure 12 shows the results for the long exposures of both NGC 104 and NGC 6791. Figure 13 shows the same for short exposures. The plots are divided by whether the observations were post-flashed with 12 e-/pix and by whether they were corrected with the CTE correction software (Anderson, 2011). Additional flash levels (6, 18, 24, 33, 55, 91, and 116 e-/pix) for NGC 104 are plotted in Figures 27 - 33 in Appendix D. They show that after ~12 e-/pix, one can still gain back flux, but not shown is that it comes with costs, such as increase in noise; see Anderson et al. (2012) and the forthcoming Anderson (2017).

For the long exposures (here, ~400 s) in Figure 12, the CTE correction software corrects flux losses to under 0.1 e-/2048 pixels at a steady rate over time. The lowest flux bin (500-2000 e-) in the short exposures (~30-60 s) in Figure 13, however, shows an uptick in flux loss even with the correction software applied starting in ~2015 (~57000 MJD); it seems that this level of source flux is becoming unrecoverable. The plots further illustrate that

the best approach for controlling CTE-induced flux losses is to both use a post-flash of at least 12 e-/pix and to apply the CTE correction software, although the CTE correction can sometimes over-correct by a few percent.
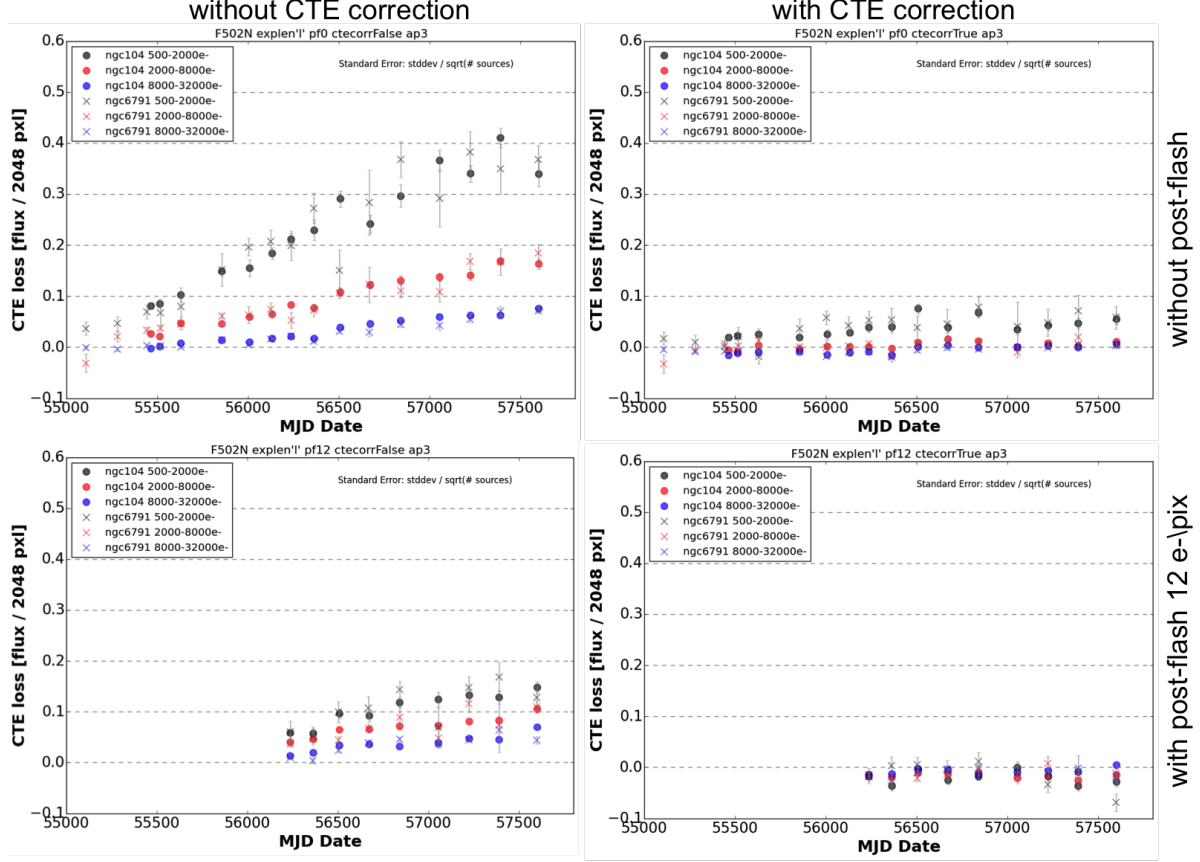

Figure 12 – Change in CTE losses seen in long exposures, without post-flash (top) and with 12 e-/pix post-flash (bottom). Results without the pixel-based CTE correction are to the left and results with CTE-correction are to the right. The circles represent the NGC 104 observations and the Xs represent the NGC 6791 observations. Each color is a different flux bin. There are no data points for post-flash before ∼56250 MJD (mid-Nov. 2012) because the mode was not yet used in general observations. As discussed in the text, there appears to be a plateau in CTE loss starting around ∼57000 MJD.

The rate of CTE loss appears to be reaching a plateau starting around late 2014 (∼57000 MJD), except perhaps in the lowest flux bin in the short exposures. A smaller flattening is seen in the mid-2011 - mid-2013 (∼55750 - 56500 MJD) data. Noeske et al. (2012) tentatively attributed this flattening to increasing Solar activity following the 2008 minimum. Increased Solar activity has been linked to decreases in CCD cosmic ray damage (Fürst et al., 2009). The majority of the damage to the UVIS CCDs is thought to occur in the South Atlantic Anomaly (SAA), a zone of high radiation, which HST passes through ∼8 times per day (Janesick (2001), Barker et al. (2010)). When Solar activity is high, it heats the upper

atmosphere, increasing the neutral atmospheric density at the SAA's altitude, and therefore providing the CCDs extra shielding from cosmic rays. Solar activity has been linked to long-term trends seen on other HST instruments, such as with WFPC2's cosmic-ray-induced dark current evolution (McMaster et al., 2008, Chapter 4.8). The current Solar cycle's maximum occurred in 2014 (Hathaway, 2016) and it may be that the UVIS chips are in a grace period before Solar activity again drops and radiation damage begins to accumulate once more at pre-2014 rates.
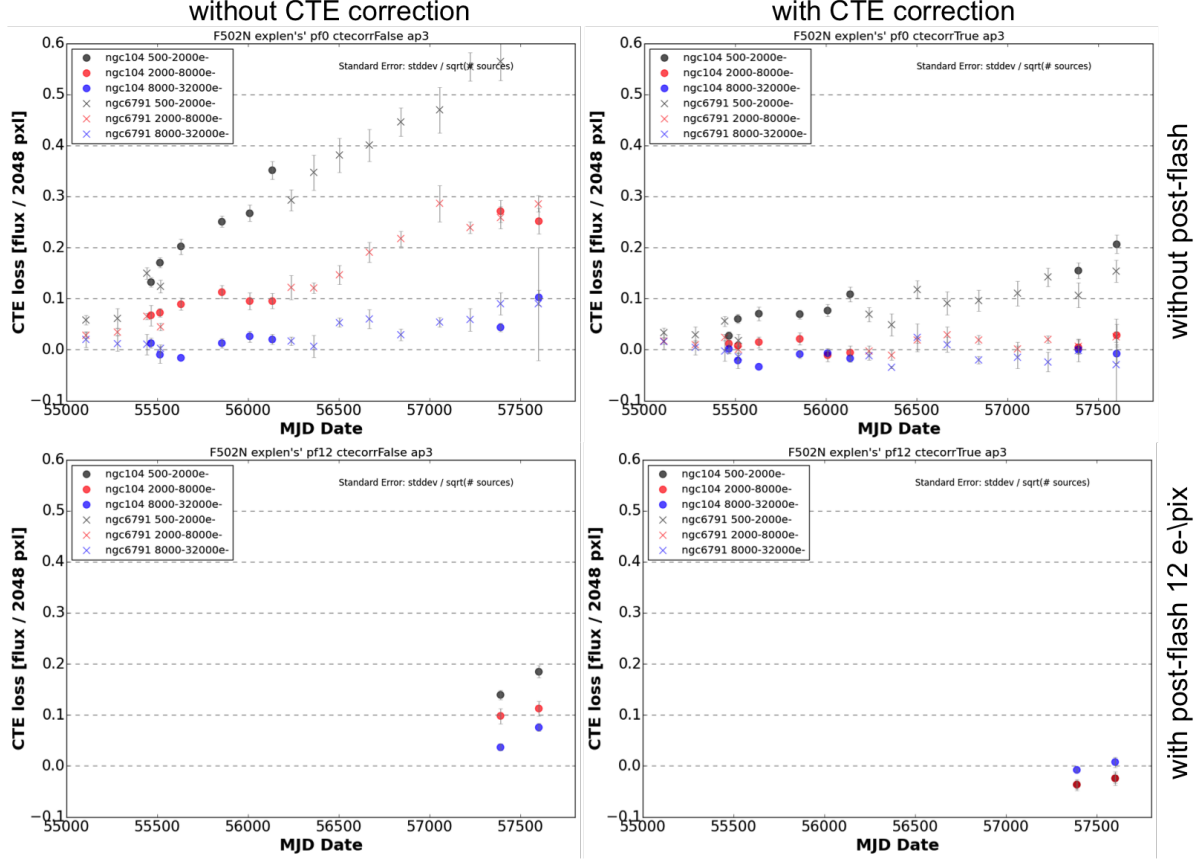
Figure 13 – Same as for Figure 12 but for short exposures (30-60 s). Between Nov. 2012 and Jan. 2016 the monitor had not been taking short exposures of field NGC 104, and up to Jan. 2016 had taken no post-flashed short exposures.

In addition to CTE losses, it is known that there are other, smaller sources of degradation in the detector's sensitivity, which appear dependent on wavelength. From over two years of available white dwarf (GRW+70) monitor data, 1% flux declines have been found on UVIS2 in F502N, and from 7 years of data, 2% flux declines on both chips in F606W (Gosmeyer et al. (2014), Shanahan et al. (2017)). The cause of this sensitivity decline is unknown. It should also be noted that the two UVIS chips are combined in this measurement of

CTE loss, although it is known that the two chips, cut from different wafers, have subtle differences in aging and likely had different charge trap distributions at manufacture (WFC3 CCD Milestone Review, 2001). The different CTE losses per chip are discussed in Gosmeyer and Baggett (2016). With these caveats in mind, observers are cautioned against taking individual reported numbers as absolute CTE loss measurements.

CTE Evolution with Flash Level

We plot the flux loss per 2048 pixels due to CTE degradation against commanded flash level in electrons. Figure 14 shows the data without the CTE correction and Figure 15 shows the data with the CTE correction. Table 2 summarizes the epochs when a given flash level was observed. At the highest flux bin (8000-32000 e-) in Figure 15, CTE loss appears negligible across all flash levels. The CTE correction can slightly over-correct (on the plots, pull the CTE loss below 0) images that have been post-flashed.

The source flux regained from post-flashing the image hits a "sweet spot" around 12 e-/pix (vertical red line) and then slowly levels off, confirming the conclusions of Anderson et al. (2012). The higher values of CTE loss before 12 e-/pix in Figure 15 suggest that even with CTE correction, users should use a post-flash that brings background to at least 12 e-/pix. Beyond 12 e-/pix, CTE loss continues to show improvement, which appears to settle around 30 e-/pix. The Appendix D Figures 27 - 33 suggest much the same, that there is a slow leveling off of source recovery following 12 e-/pix. The costs and benefits of post-flashing over 12 e-/pix will be investigated in a coming report (Anderson, 2017).
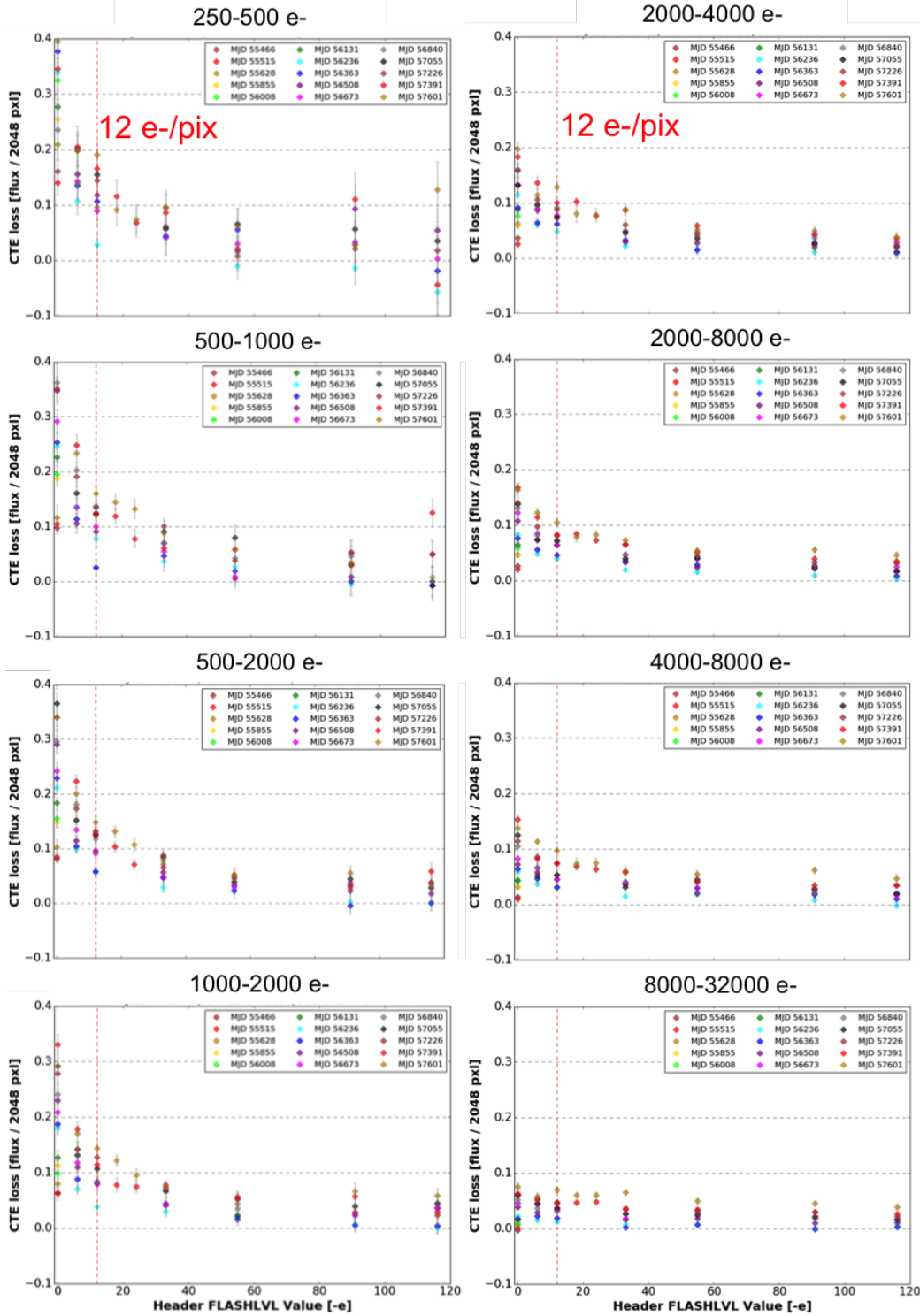
Figure 14 – *The flux loss per 2048 pixels against commanded flash level in electrons, without CTE correction. Each point is a measurement from a different epoch. Each subplot contains one of eight flux bins ranging from 250-500 e- to 8000-32000 e-. The red dotted line marks the current minimum recommended image background level (12 e-/pix). These data are only available for filter F502N, target NGC 104, long exposure of 348 seconds, dating after November 2012.*
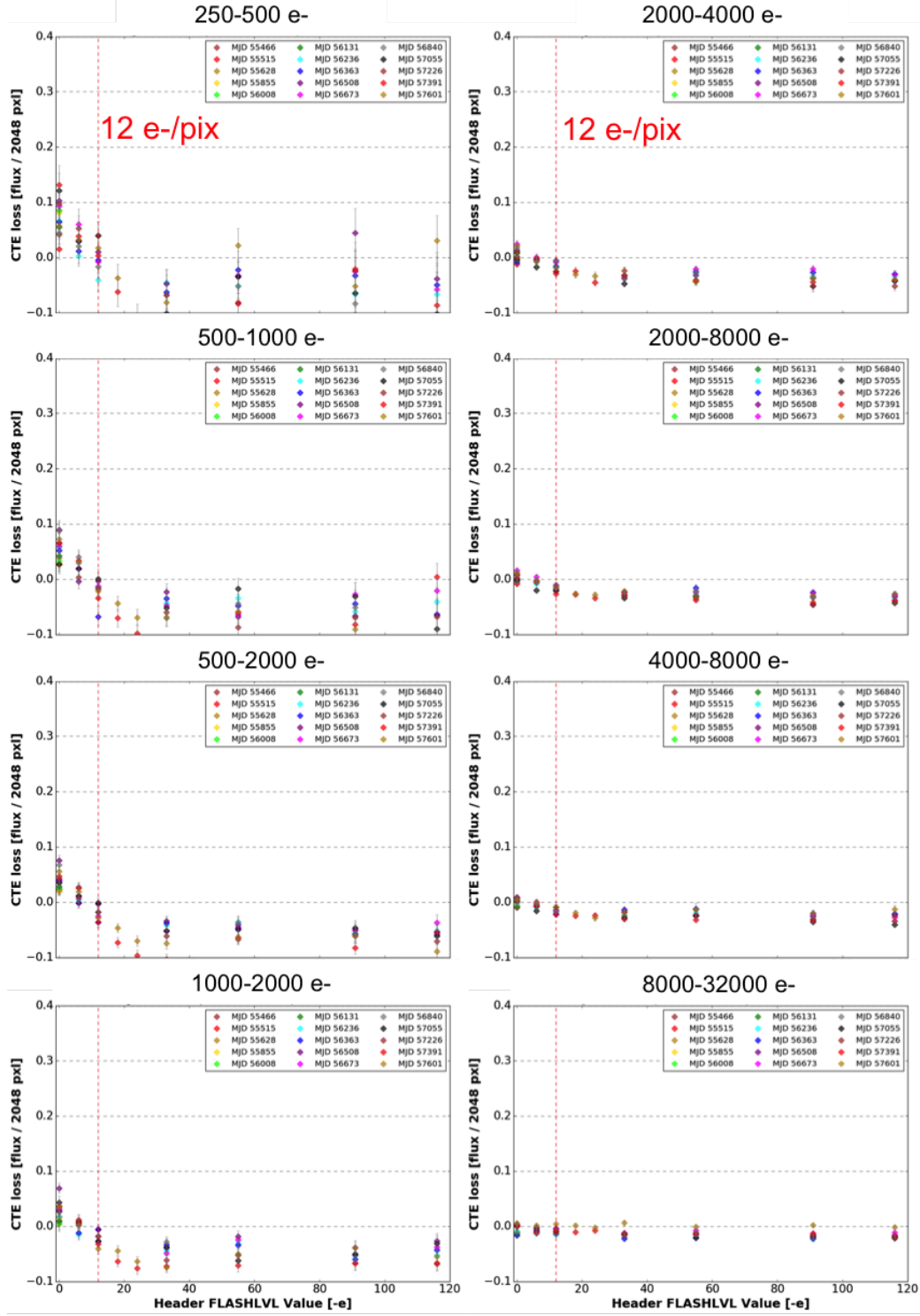
Figure 15 – Same as Figure 14 but with CTE correction.

Source Recovery

Figure 16 illustrates the gains in source recovery by using CTE-corrected data for a subset of epochs. At the lowest flux bins, applying the CTE correction can recover up to 50% of sources. Comparing the right plot (with post-flash 12 e-/pix) to the left (without post-flash), it is apparent post-flash, combined with the CTE correction, gives a higher source recovery, almost 90% in the lowest bins, whereas without post-flash one can hope to recover only up to 50% in the July 2015 epoch (triangles). Additional examples can be found in the Appendix B tables of Gosmeyer and Baggett (2016) that list the numbers of sources recovered in eight flux bins for the six image pairs used for that study.
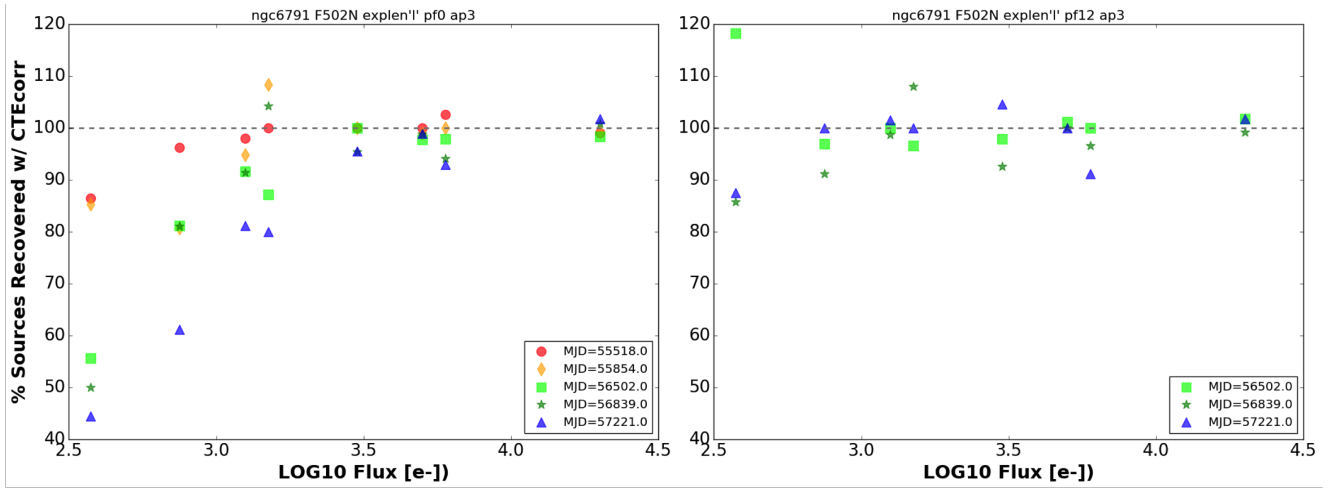
Figure 16 – Illustration of the percent sources recovered (in the FLT relative to the FLC) in a subset of epochs for NGC 6791. The non-post-flashed dataset is left and the 12 e-/pix post-flash dataset is right. Some flux bins show gains in over 100% probably because the CTE correction pushed sources into a neighboring bin.

Conclusions

In this report we have summarized the evolution of the charge transfer efficiency (CTE) of the WFC3/UVIS detector and the methods used to monitor it since 2009, using observations of star clusters NGC 104 and NGC 6791 taken in various observational modes (long and short exposure times, and various background levels) and processing steps (with and without the pixel-based CTE correction software). These data are used to inform users of the best possible combinations of pre- and post-observational strategies that will mitigate CTE loss in their data and to serve as a check on the performance of the pixel-based CTE correction software.

We have described our transition of the analysis pipeline from `IDL/IRAF/Fortran` to `Python`. The re-written pipeline improves the cross-identification of sources and stores all photometric results in a `SQLite` database, which enables a more robust analysis to be performed on the CTE monitor's nominal data, as well as makes simpler the processing of non-nominal data (e.g., flash levels 6, 18, 24, 33, 55, 91, and 116 e-/pix). We hope the consolidation of languages into a single one, the now-standard `Python`, will make the code base easier to maintain and pass on to future inheritors of the monitoring program. The analysis pipeline is general enough that it might be adopted by the HST/Advanced Camera for Surveys (ACS) team, who have a similar external CTE monitor program for ACS/WFC, and the photometry database may be useful to WFC3 team members for other studies, such as photometric or shutter trends.

We have made the latest F502N coefficients for the empirical photometric correction formula available in Table 1 and observers can input them into Equation 2 with their source's flux, observation epoch, and pixel distance from the readout amplifier to get an approximate value of CTE loss in their point-source photometry. Users should use coefficients derived from conditions – background levels being most important – that most closely match their observations. The coefficients reported here were derived from data spanning from October 2009 to August 2016, calibrated with `calwf3 v3.3`. The expansion of the correction formula was printed inaccurately in previous reports and users should instead refer to the expansion in Equation 2 of this report. The coefficients from this and previous CTE reports can be downloaded as text files from http://www.stsci.edu/hst/wfc3/ins_performance/CTE/. We are also working on making an online calculator for the correction formula.

CTE losses appear to be flattening out with increasing Solar activity, as predicted in Noeske et al. (2012). We are starting to see an unrecoverable population of low-flux sources in the short exposure data, even with the CTE correction applied. We verify that 12 e-/pix is still an appropriate flash level for images and flashing at a higher level, up to around 30 e-/pix, yields an additional but small increase in sources' flux counts. We show that applying the CTE correction to a non-post-flashed image can recover nearly 50% of sources at the low flux end. In post-flashed data, where the CTE loss has already been partially mitigated, the CTE correction can recover nearly 10% of sources at the low flux end.

Users should be aware that all CTE measurements presented here actually are a blend of the two UVIS chips. In a separate instrument science report (Gosmeyer and Baggett, 2016) we analyze a dataset that measures CTE loss per-chip.

Future work will finish transitioning photometry from `IRAF/DAOPHOT` (the last non-`Python` piece of the CTE monitor pipeline) to the the `Python` photometry package `Photutils`. We expect cleaning cosmic rays will tighten the scatter in the flux-ratio vs y-position plots, from

which we derive our CTE loss measurements, and so we will investigate incorporating some type of cosmic ray-rejector. We will look into incorporating proper motion into the F502N master catalogs of the two clusters. Finally, we will create master catalogs using the pre-2012 F606W images in order to include sources only visible in the wide-band filter and thus complete our photometry database for this monitor.

Software Notes

Our data processing and analysis relied on the following `Python` packages:

- `astropy`, v1.1.dev, http://www.astropy.org/

- `drizzlepac`, v2.1.1.dev48001, http://drizzlepac.stsci.edu/

- `matplotlib`, v1.4.2, http://matplotlib.org/

- `numpy`, v1.9.1, http://www.numpy.org/

- `photutils`, v0.1, https://photutils.readthedocs.io/en/latest/

- `pyraf`, v2.2.dev2514, http://www.stsci.edu/institute/software_hardware/pyraf

- `sqlalchemy`, v1.0.8, http://www.sqlalchemy.org/

Calibration of the data was performed through the Mikulski Archive for Space Telescopes (https://archive.stsci.edu/) using the WFC3 calibration pipeline `calwf3 v3.3`, http://www.stsci.edu/hst/wfc3/pipeline/wfc3_pipeline.

The source code for our analysis software is kept on an STScI-based server of `github`. For access or more information, email the author `cgosmeyer@stsci.edu`.

Acknowledgements

We thank K. Noeske for laying the foundation of the monitor's analysis pipeline; R. Avila for unrelenting help on all things AstroDrizzle; V. Bajaj for being agreeable and quick about getting to the bottom of the IRAF-Python photometry discrepancy; D. Borncamp for insights into database schemas; M. Bourque for discussions about databases and for excellent example code; M. Gennaro for the critique of WFC3 ISR 2016-17 that led us to recheck how we measure CTE and ultimately give us more confidence in our method; and V. Platais for the thorough review of this report.

References

Anderson, J. (2011). CTE Tools. http://www.stsci.edu/hst/wfc3/tools/cte_tools.

Anderson, J. (2017). in prep.

Anderson, J., MacKenty, J., Baggett, S., and Noeske, K. (2012). The Efficacy of Post-Flashing for Mitigating CTE-Losses in WFC3/UVIS Images. http://www.stsci.edu/hst/wfc3/ins_performance/CTE/ANDERSON_UVIS_POSTFLASH_EFFICACY.pdf.

Baggett, S., Gosmeyer, C., and Noeske, K. (2015). WFC3/UVIS Charge Transfer Efficiency 2009 - 2015. *WFC3 Instrument Science Report 2015-03*.

Bajaj, V. and Khandrika, H. (2017). *in prep.*

Barker, E. A., McCullough, P., and Martel, A. R. (2010). WFC3 IR SAA Passage Behavior. *WFC3 Instrument Science Report 2009-40*.

Chiaberge, M. (2012). A new accurate CTE photometric correction formula for ACS/WFC. *Instrument Science Report ACS 2012-05*.

Davis, L. (1987). Specifications for the Aperture Photometry Package. http://iraf.net/irafdocs/apspec.pdf.

Deustua, S., editor (2016). *WFC3 Data Handbook, Version 3.0*. Baltimore: STScI.

Fürst, F., Wilms, J., Rothschild, R. E., Pottschmidt, K., Smith, D. M., and Lingenfelter, R. (2009). Temporal variations of strength and location of the South Atlantic Anomaly as measured by RXTE. *Earth & Planetary Science Letters*.

Gosmeyer, C. and Baggett, S. (2016). WFC3/UVIS External CTE Monitor: Single-Chip CTE Measurements. *WFC3 Instrument Science Report 2016-17*.

Gosmeyer, C., Baggett, S., Deustua, S., and Hammer, D. M. (2014). Update on the WFC3/UVIS Stability and Contamination Monitor. *WFC3 Instrument Science Report 2014-20*.

Hathaway, D. (2016). Solar cycle prediction. http://solarscience.msfc.nasa.gov/predict.shtml.

Janesick, J. (2001). *Scientific Charge-coupled Devices*. SPIE Press.

Khandrika, H., Baggett, S., and Bowers, A. (2016). WFC3/UVIS EPER CTE Cycles Aug 2009 - Apr 2016. *WFC3 Instrument Science Report 2016-10.*

McMaster, M., Biretta, J., Baggett, S., Bedin, L., Brammer, G., Burrows, C., and Casertano, S. (2008). *WFPC2 Instrument Handbook, Version 10.0.* Baltimore: STScI.

Noeske, K., Baggett, S., Bushouse, H., Petro, L., Gilliland, R., and Khozurina-Platais, V. (2012). WFC3 UVIS Charge Transfer Efficiency October 2009 to October 2011. *WFC3 Instrument Science Report 2012-09.*

Ryan, Jr., R. E., Deustua, S., Anderson, J., Baggett, S. M., Bajaj, V., Bourque, M., Bowers, A. S., Dahlen, T., Durbin, M., Gosmeyer, C., Gunning, H., Khandrika, H., Mack, J., MacKenty, J., Martlin, C., Kozhurina-Platais, V., Sabbi, E., and Sosey, M. (2016). The Updated Calibration Pipeline for WFC3/UVIS: A Reference Guide to Calwf3 3.3. http://www.stsci.edu/hst/wfc3/documents/ISRs/WFC3-2016-01.pdf.

Shanahan, C., Gosmeyer, C., and Baggett, S. (2017). Update on the WFC3/UVIS Stability and Contamination Monitor. *WFC3 Instrument Science Report 2017-xx, in prep.*

van Dokkum, P. (2001). L.A. Cosmic. http://www.astro.yale.edu/dokkum/lacosmic/.

WFC3 CCD Milestone Review (2001). Internal NASA document.

WFC3 Team (2009). Pixel Area Maps. http://www.stsci.edu/hst/wfc3/pam/pixel_area_maps.

Appendix A: Observations

Proposal	Visits	Epochs	F502N Flashlvls [e-/pix]	F606W Flashlvls [e-/pix]	F502N Exptimes [s]	F606W Exptimes [s]
12348	1	Sep 2010	0	-	30,360	-
12379	2,8,11	Nov 2010,Mar 2011	0	0	30,348,360	30,348,350
12692	2,5,8	Oct 2011,Mar 2012,Jul 2012	0	0	30,360	30,350
13083	2,4,6	Nov 2012,Mar 2013,Aug 2013	0,6,12,33,55,91,116	-	348	-
13566	2,4	Jan 2014,Jul 2014	0,6,12,33,55,91,116	-	348	-
14012	2,4	Feb 2015,Jul 2015	0,6,12,33,55,91,116	-	348	-
14378	2,4	Jan 2016,Aug 2016	0,6,12,18,33,24,55,91,116	-	30,348	-

Table 2 – Summary of observations used in this report for the dense-field target **NGC 104**. *Proposal 12348, which tested the Charge Injection mode, was not part of the nominal monitoring program; however, we incorporate into our dataset some of this proposal's non-charge injected image pairs. Proposal 12379, Visits 07 and 14, contain non-standard fields of NGC 104 and non-standard dithers, so we do not include them in our dataset. Visit 13 of the same proposal not only was taken in Charge Injection mode, but also suffered from a guide star failure, and was therefore discarded from our dataset. Starting in Proposal 13083 images in filter F606W was dropped and images in F502N with various levels of post-flash were added in. In Proposal 14378 we again started taking short exposures with both without post-flash and with post-flash of 12 e-/pix. See the* Data Section *for more notes on observations.*

Proposal	Visits	Epochs	F502N Flashlvls [e-/pix]	F606W Flashlvls [e-/pix]	F502N Exptimes [s]	F606W Exptimes [s]
11924	1,2,3	Oct 2009,Mar 2010,Sep 2010	0	0	60,420	30,360
12379	1,9	Nov 2010,Mar 2011	0	0	60,400,420	30,348,360
12692	1,4,7	Oct 2011,Mar 2012,Jul 2012	0	0	60,420	30,360
13083	1,3,5	Nov 2012,Mar 2013,Jul 2013	0,12	-	60,420	-
13566	1,3	Jan 2014,Jul 2014	0,12	-	60,420	-
14012	1,3	Jan 2015,Jul 2015	0,12	-	60,420	-
14378	1,3	Jan 2016,Jul 2016	0,12	-	60,420	-

Table 3 – Summary of observations used in this report for the sparse-field target **NGC 6791**. *Exposure times have remained constant through all proposals. The only exception is Visit 9 in Proposal 12379, where exposure times for F502N are 60 and 400 s, and for F606W are 30 and 348 s. The filter F606W was dropped starting in Proposal 13083. We do not include the NGC 6791 observations in Proposal 14012's Visit 05, which was a test that used binning.*

Appendix B: Comparing IDL Pipeline to Python Pipeline

The most recent plots created by the original `IDL` pipeline can be found in Baggett et al. (2015). In Figure 17 we plot subsets of the `IDL` pipeline-derived CTE loss measurements over those derived from the `Python` pipeline. The agreement is good at high fluxes and diverges at low fluxes. This is likely because of the differences in their source-identifying algorithms – in the `Python` pipeline sources are identified using a master catalog, which will plop an aperture onto a faint source however much it may be overwhelmed by CTE trailing or background, whereas in the `IDL` pipeline sources are found image-to-image using `IRAF/DAOFIND`, which will not identify a faint source once it crosses a given threshold.
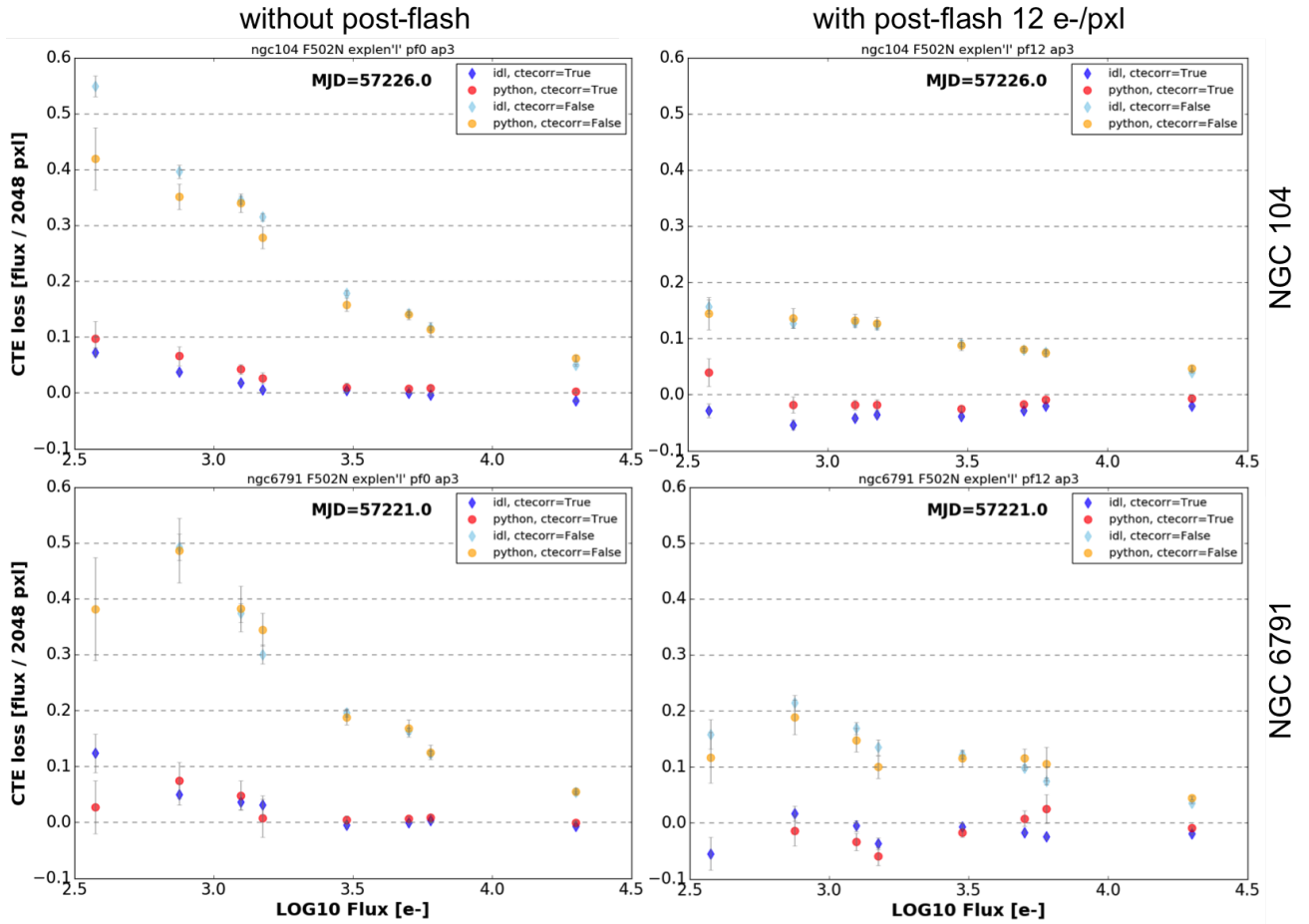
Figure 17 – Comparing the `IDL` *pipeline's CTE loss measurements per log10 flux bin to the new* `Python` *pipeline's, for non- and CTE-corrected data, with (right) and without (left) post-flash 12 e-/pix. NGC 104 is in the top two panels and NGC 6791 is in the bottom two. Both pipelines used* `IRAF/DAOPHOT` *photometry.*

In Figures 18 (`Python` pipeline) and 19 (`IDL` pipeline), we compare the CTE loss model values derived from Equation 1 using each pipeline's most recent coefficients to the values

calculated from the pixel-based CTE correction software. Users may be interested to note that the CTE loss given by the correction formula is never over-estimated, as is sometimes the case for the CTE correction software. Users therefore may find it beneficial, in some cases, to do their point-source photometry on FLTs and correct their values with the formula, over doing photometry on the software-corrected FLCs.
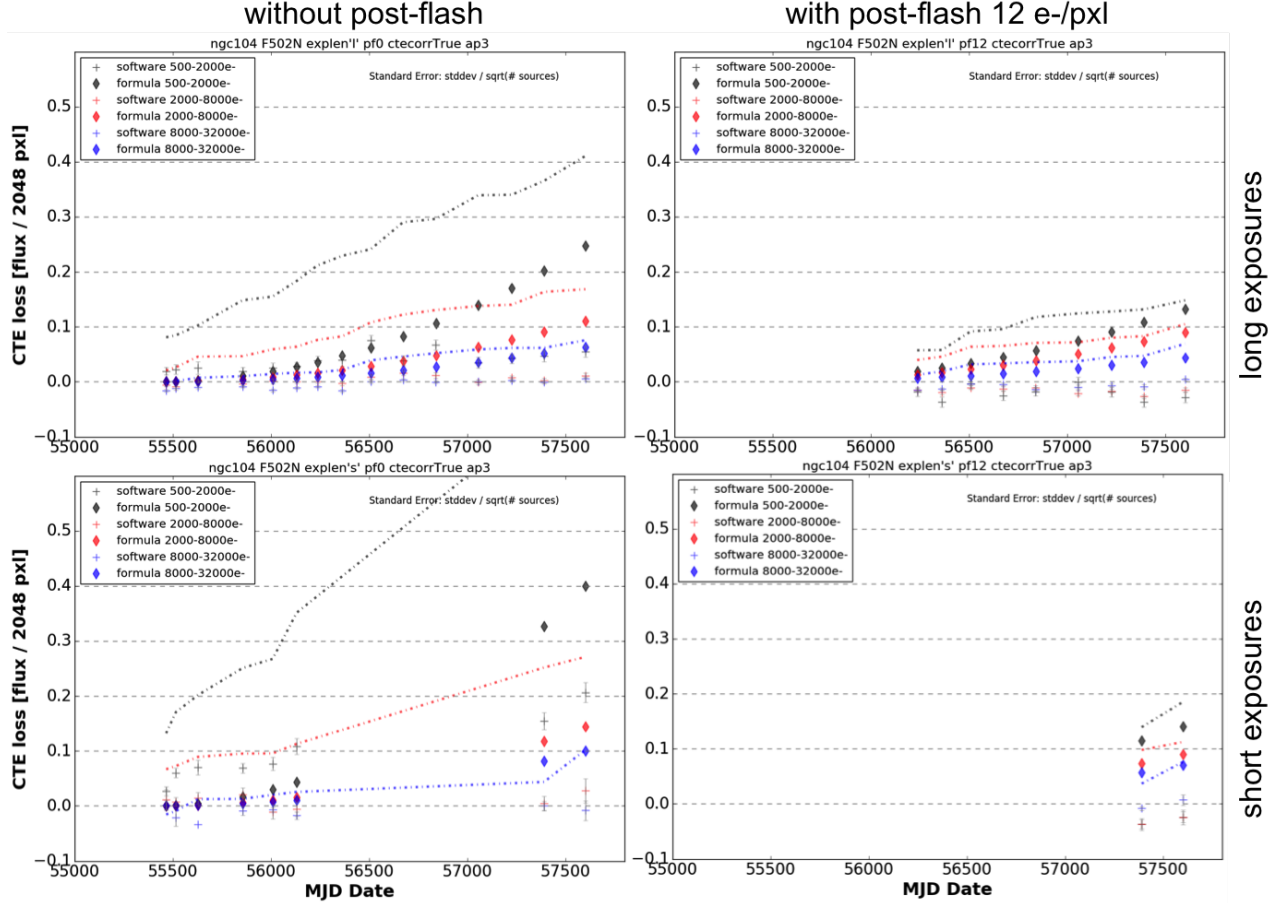
Figure 18 – Verifying that Equation 1 with coefficients derived from the `Python` pipeline can ameliorate CTE loss. Shown here are a subset of the datasets of NGC 104 in filter F502N, non-post-flashed values at left and post-flash 12 e-/pix values at right. The filled diamonds represent CTE loss values derived from the empirical model, using the average of the flux bin in f, the epoch in d, and coefficients from the upper NGC 104 columns of Table 1. The crosses represent observational data on which the CTE correction software was applied. The dash-dot lines represent observational data without CTE correction.

A downside to the `Python` pipeline is that we cannot reproduce the F606W plots. The cause is likely to be that the master catalog was created from F502N images. The stars found in the narrow-band filter saturate for the most part in the long-exposure of the wide-band filter, and that makes them fall completely out of even the highest flux bins, and therefore out of the plots. In future work we could, if time allows, expand the master catalogs for

this case. It is not high priority because observations for F606W were discontinued in 2012. They were taken in the first few cycles because of their relatively high image background; they have now been replaced with appropriately post-flashed F502N data. For empirical correction coefficients for the F606W data, see Table 1 in Baggett et al. (2015).
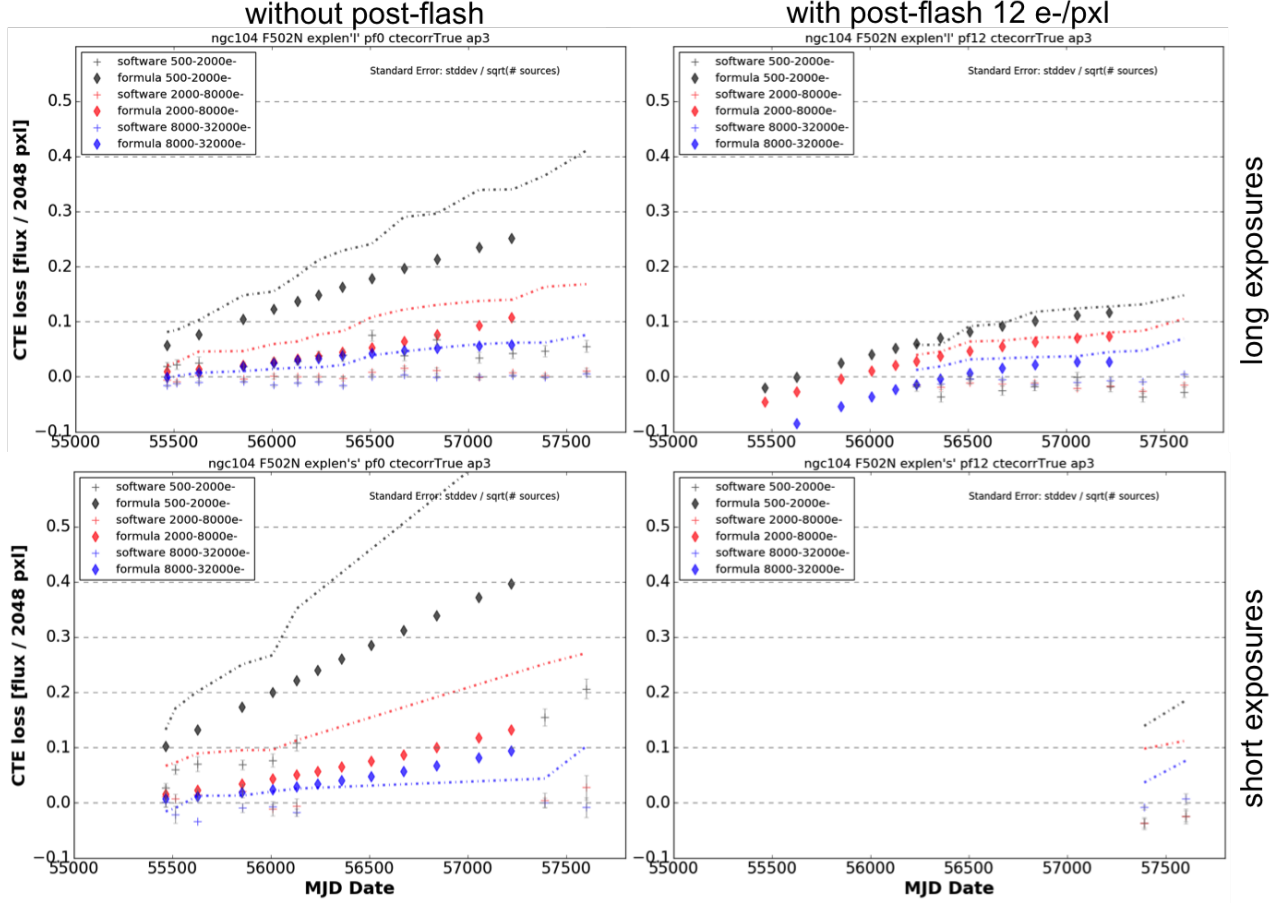
Figure 19 – Similar to Figure 18 but here the filled diamonds represent values calculated using coefficients derived from the IDL pipeline, published in Table 1 of Baggett et al. (2015). We stop plotting the model CTE losses at the last two epochs since those were never run through the IDL pipeline; for the same reason the lower right panel is empty of photometric-corrected points.

Appendix C: Additional Plots of CTE Evolution with Log10 Flux
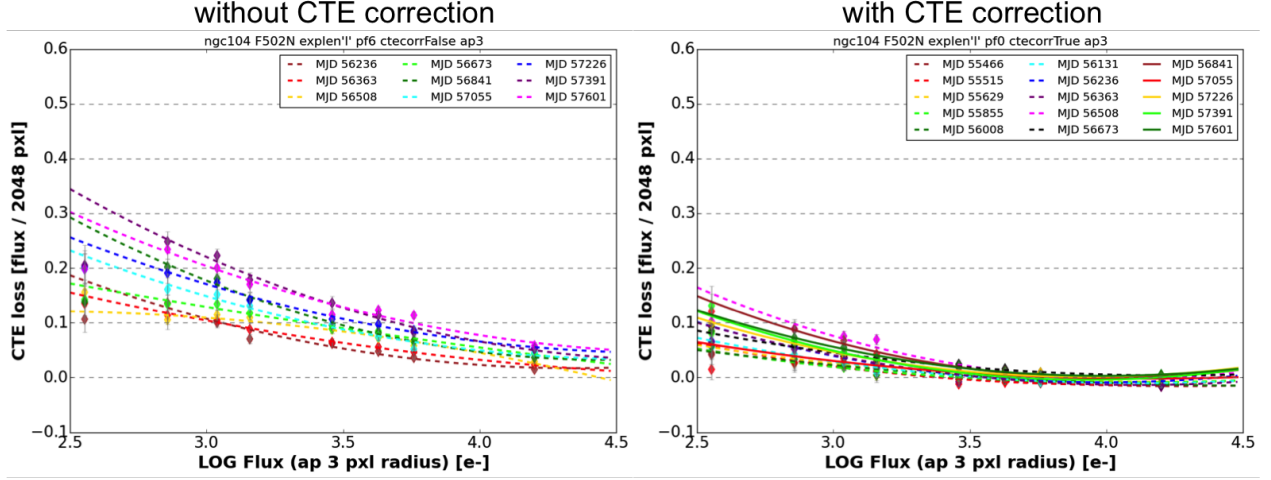
*Figure 20 – Similar to Figure 8 but with post-flash **6 e-/pix**.*
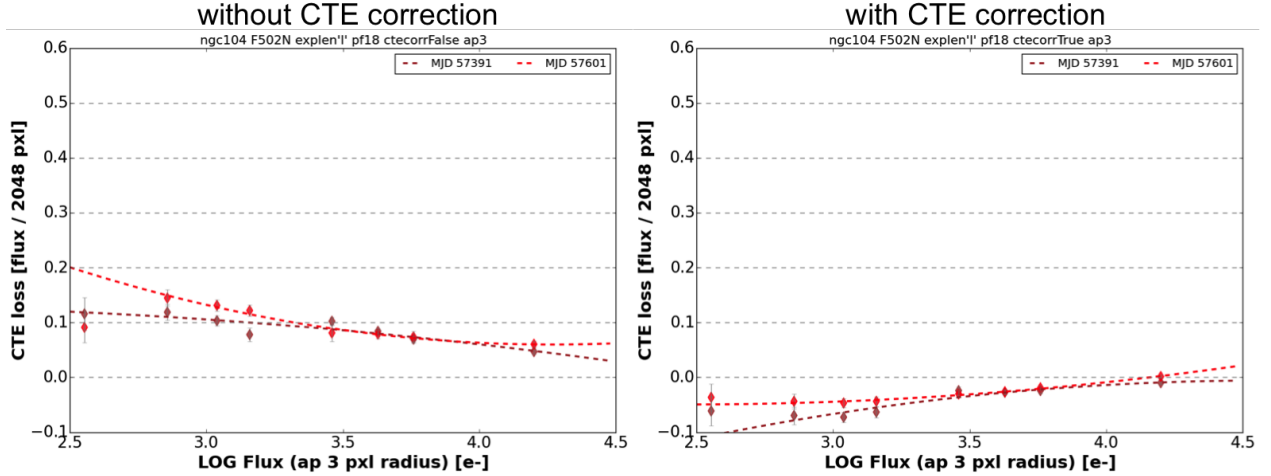
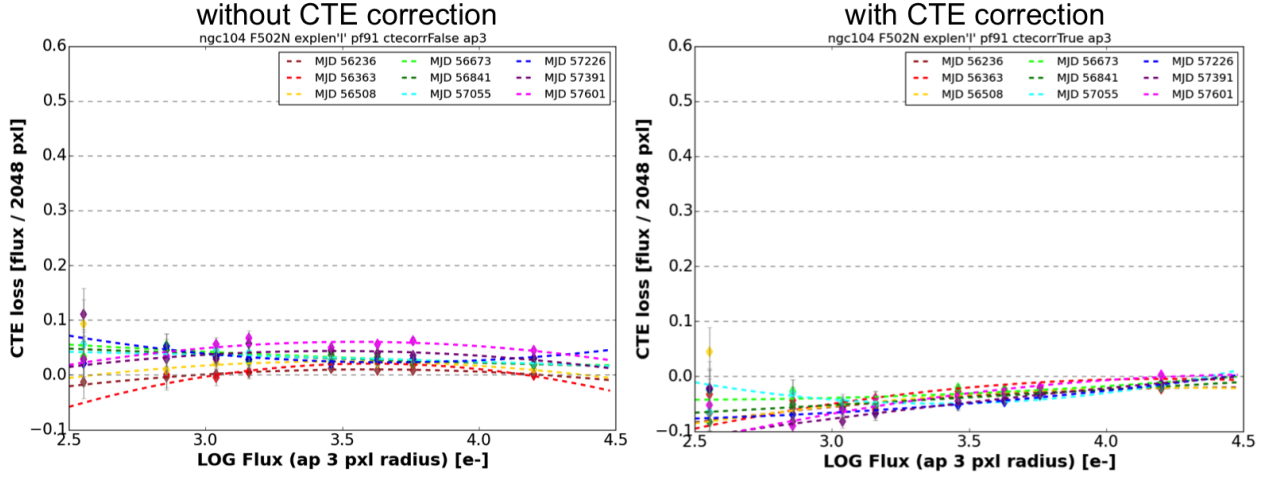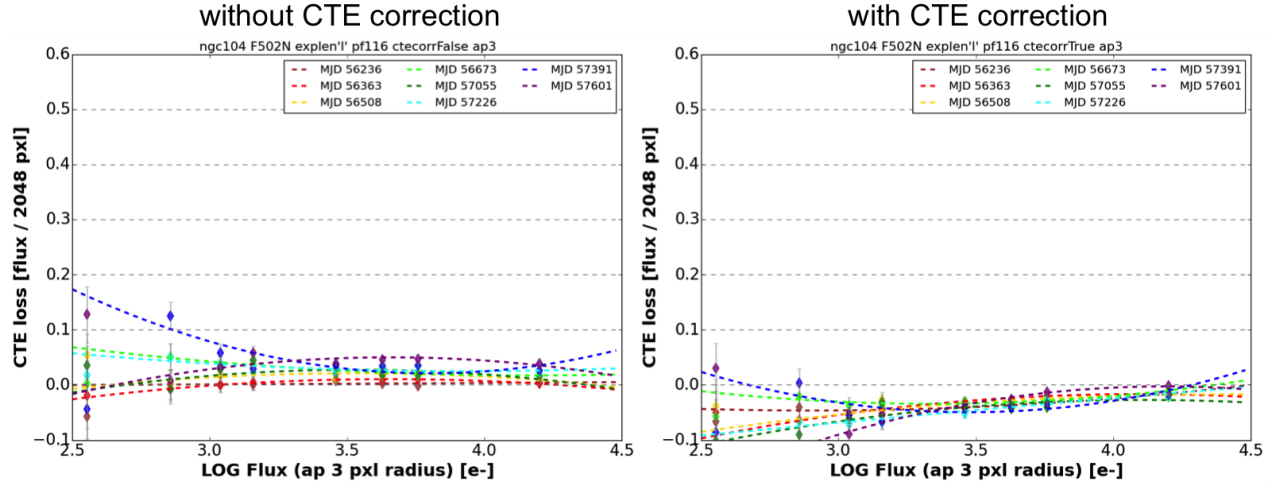*Figure 21 – Similar to Figure 8 but with post-flash **18 e-/pix**.*

without CTE correction

with CTE correction
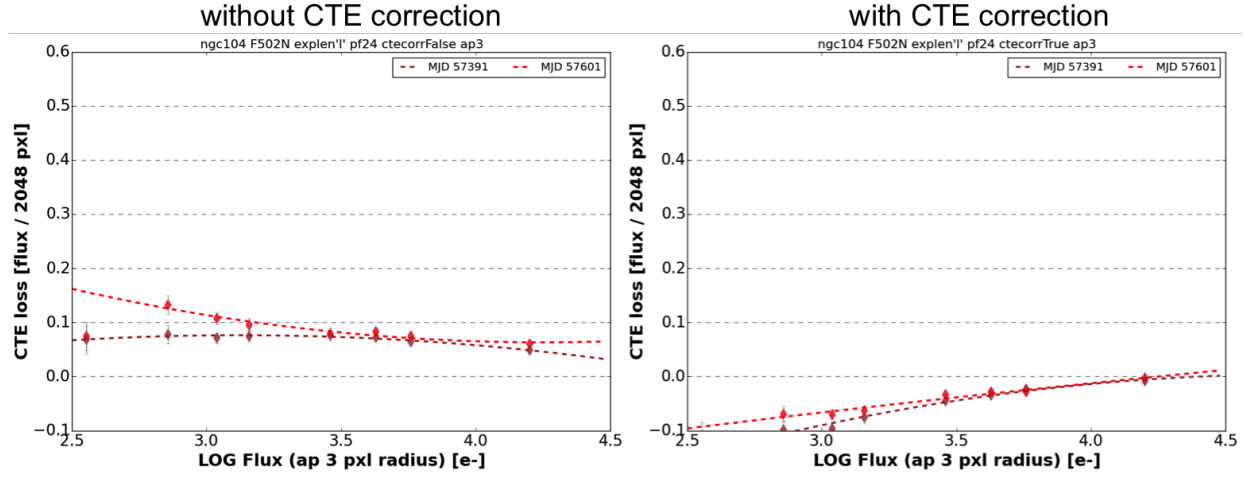
Figure 22 – Similar to Figure 8 but with post-flash **24 e-/pix**.

without CTE correction

with CTE correction
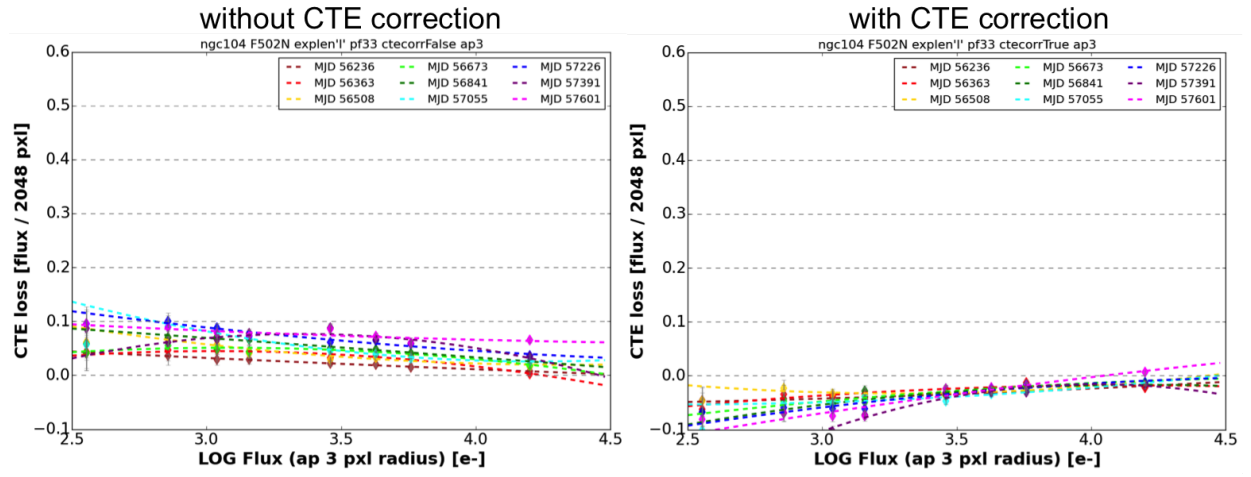
Figure 23 – Similar to Figure 8 but with post-flash **33 e-/pix**.
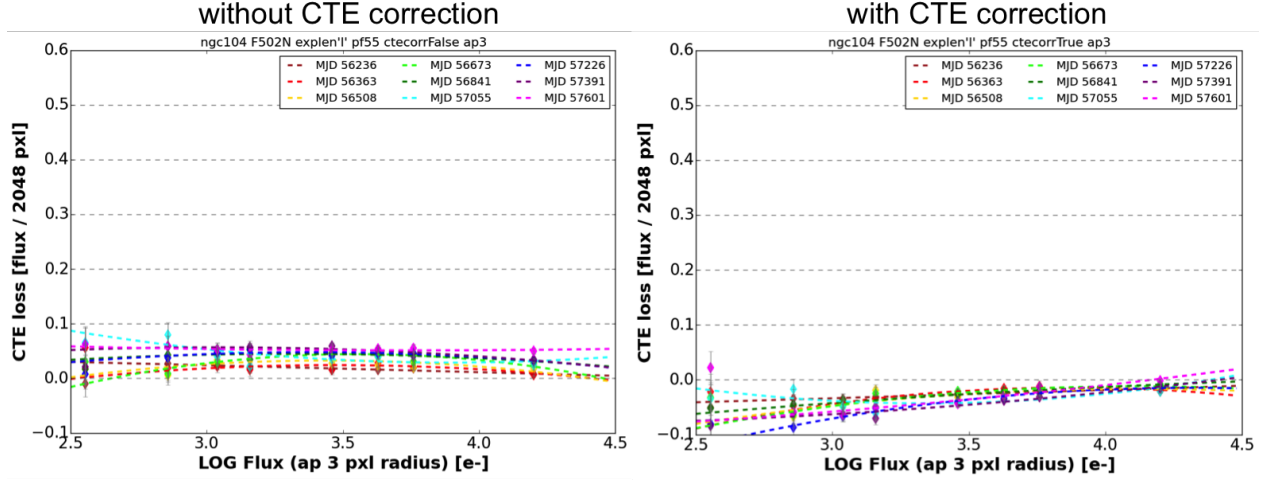
*Figure 24 – Similar to Figure 8 but with post-flash **55 e-/pix**.*

*Figure 25 – Similar to Figure 8 but with post-flash **91 e-/pix**.*

*Figure 26 – Similar to Figure 8 but with post-flash **116 e-/pix**.*

Appendix D: Additional Plots of CTE Evolution with Time
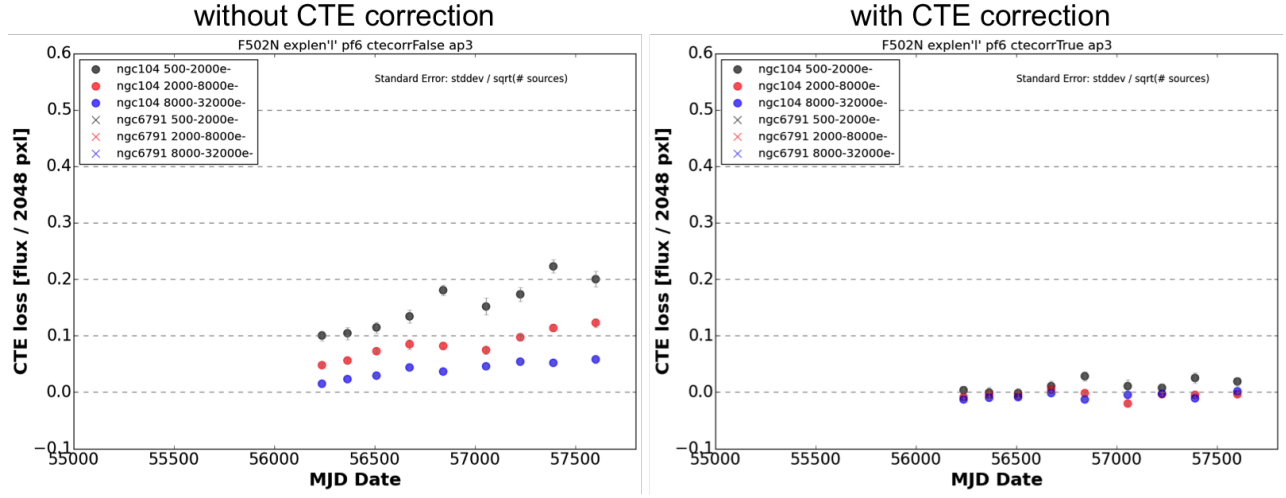
*Figure 27 – Similar to Figure 12 but with post-flash **6 e-/pix**. There are no short exposures for this flash level and only observations of NGC 104.*
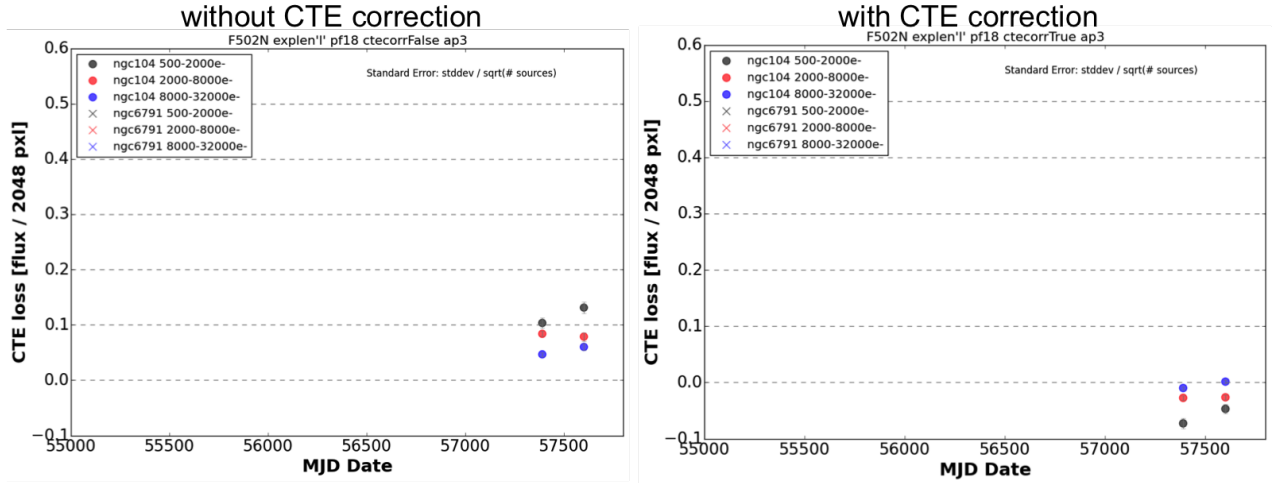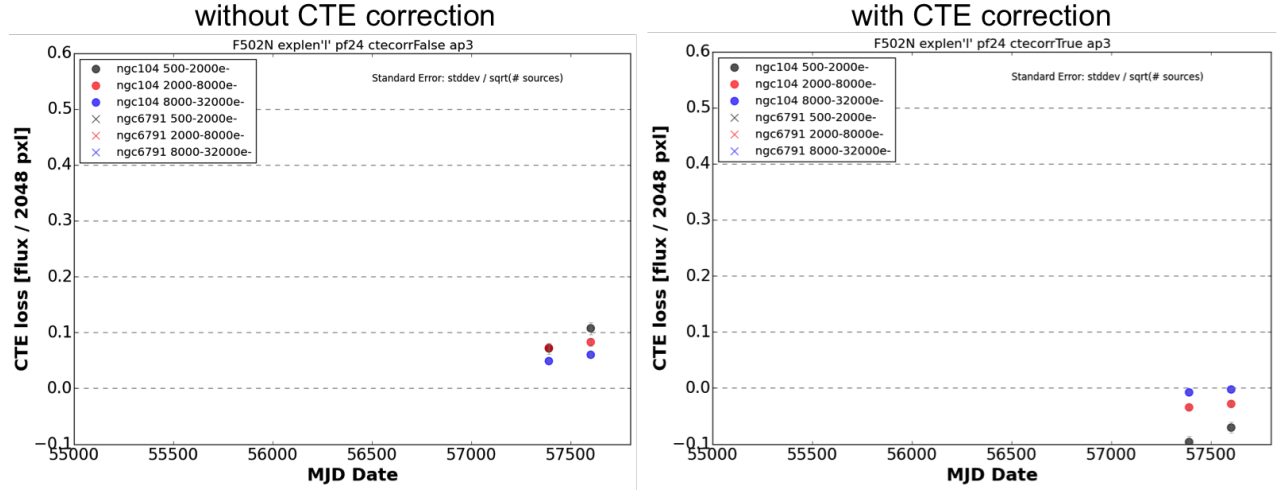

*Figure 28 – Same as Figure 27 but for post-flash **18 e-/pix**.*

without CTE correction

with CTE correction

Figure 29 – Same as Figure 27 but for post-flash **24 e-/pix**.

without CTE correction

with CTE correction
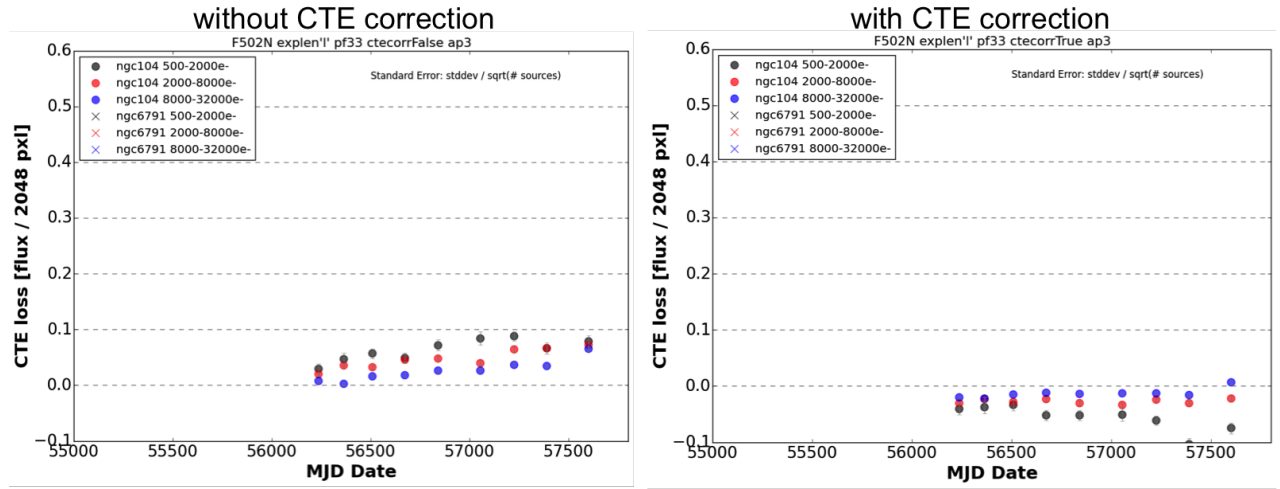
Figure 30 – Same as Figure 27 but for post-flash **33 e-/pix**.
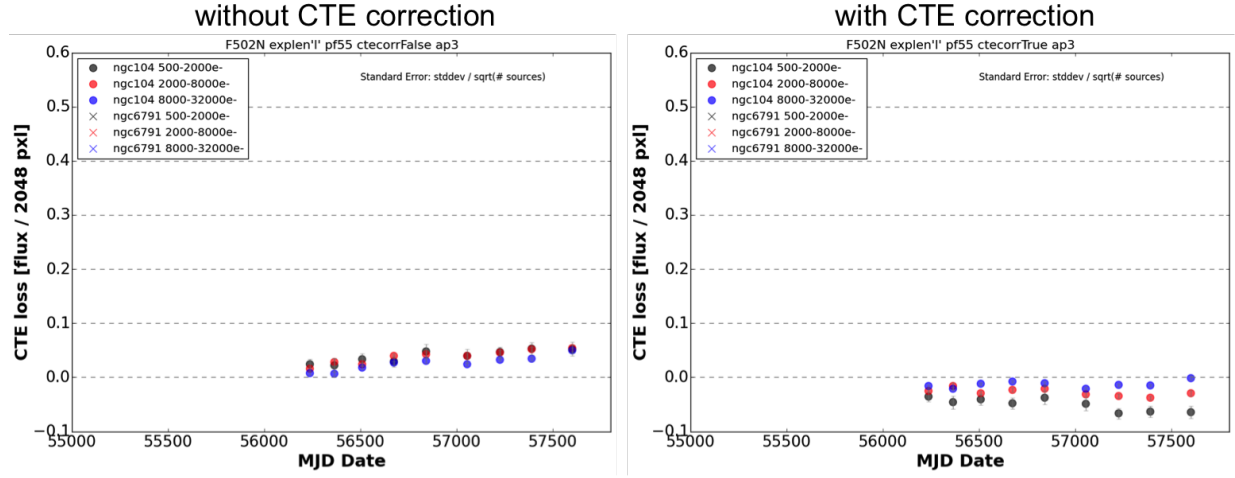
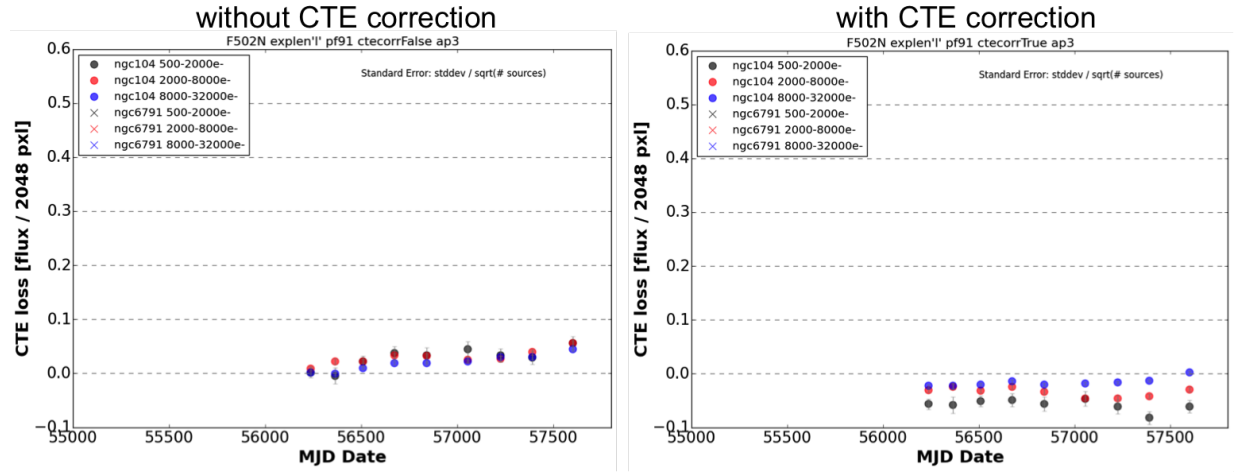*Figure 31 – Same as Figure 27 but for post-flash* **55 e-/pix**.

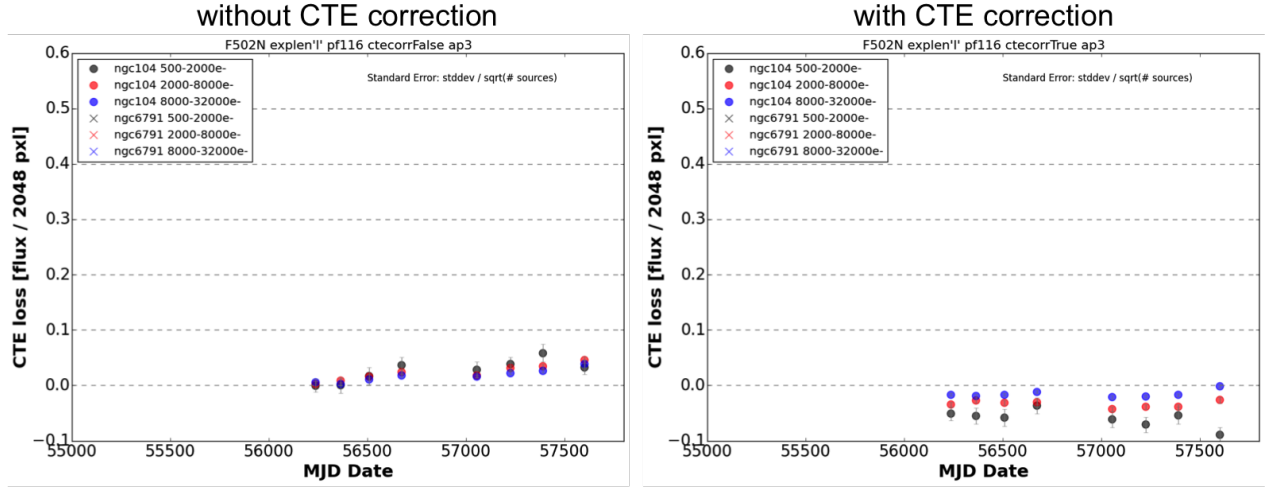*Figure 32 – Same as Figure 27 but for post-flash* **91 e-/pix**.

41

*Figure 33 – Same as Figure 27 but for post-flash **116 e-/pix**.*